

Fluid Flow and Magnet Simulation in a Gearbox

Thesis project at Chalmers in collaboration with Volvo Group and Sigma Energy & Marine (SEM)

Master's thesis in Applied Mechanics

SHREYAS VIJAYENDRA KUMAR

CHALMERS UNIVERSITY OF TECHNOLOGY
Gothenburg, Sweden 2021
www.chalmers.se

MASTER'S THESIS 2021

Fluid Flow and Magnet Simulation in a Model Gearbox

Thesis project at Chalmers in collaboration with Volvo Group and
Sigma Energy & Marine (SEM)

Shreyas Vijayendra Kumar



CHALMERS
UNIVERSITY OF TECHNOLOGY

Department of Mechanics and Maritime Sciences
CHALMERS UNIVERSITY OF TECHNOLOGY
Gothenburg, Sweden 2021

Fluid Flow and Magnet Simulation in a Gearbox
Shreyas Vijayendra Kumar

© Shreyas Vijayendra Kumar, 2021.

Supervisor: Emelie Wallenstein, SIGMA Energy and Marine
Co-Supervisor: Henrik Hagerman and Maria Petersson, Volvo Group AB
Hua-Dong Yao, Mechanics and Maritime sciences, Chalmers University of Technology
Examiner: Hua-Dong Yao, Mechanics and Maritime sciences, Chalmers University of Technology

Master's Thesis 2021
Department of Mechanics and Maritime sciences
Chalmers University of Technology
SE-412 96 Gothenburg
Telephone +46 31 772 1000

Printed by Chalmers Reproservice
Gothenburg, Sweden 2021

Fluid Flow and Magnet Simulation in a Gearbox

Shreyas Vijayendra Kumar
Department of Mechanics and Maritime sciences
Chalmers University of Technology

Abstract

Essential components in a transmission system such as gears, bearings and shafts are prone to damage and degradation due to frictional contact between them. Frictional contact between the mechanical components produces wear and eventually leads to breakdown of the gearbox. Lubricants are used to prevent excessive wear and early failure of the gearbox. Nevertheless, wear in a gearbox is unavoidable. If it is left unchecked, it produces more debris and increase the rate of wear leading to an increase in the maintenance cost of the lubricant. One possible methods to reduce the wear rate is to place a magnet in the gearbox as a measure to ensure cleanliness of the lubricant. The magnet is intended to capture and retain the wear debris.

This thesis aims to combine fluid flow and magnetic simulation in a gearbox using commercial software (Star CCM+) and also provide information regarding the best placement of the magnet in the gearbox. As the flow velocity and the domain size is high, unrealistic remanent flux density is implemented so that the particles are attracted to the magnet by overcoming the hydrodynamic forces. Different particle sensitivity analysis have been conducted to understand the particle accumulation in the domain. The magnet is suggested to be positioned in the last right region of the gearbox as more particles are accumulated in this region irrespective of from where the particles are injected or any small change in size and shape of the particles. The flow inside the gearbox makes the particles move towards the magnet without much resistance. The magnet does not have to do much work to attract the particles. Hence positioning the magnet in this region reduces the rate of wear inside the gearbox.

Keywords: CFD, Magnetic simulation, Lagrangian multiphase approach, wear debris, Gearbox, Star CCM+.

Acknowledgements

First and foremost, I would like to thank Volvo Group and Sigma Energy & Marine for providing me an opportunity to work on this thesis. I would also like to extend my gratitude to Emelie Wallenstein, Henrik Hagerman, Maria Petersson and Hua-Dong Yao for providing constructive suggestions for the success of this thesis. Furthermore, I am grateful to all my professors for fueling my passion in CFD.

Special thanks to Emelie Wallenstein and Christoffer Håkansson for constantly supporting and guiding me in the right direction throughout the thesis. I am grateful for them for sharing their expert knowledge in the field.

Lastly, I would like to thank my family and friends for their unconditional and loving support.

Shreyas Vijayendra Kumar, Gothenburg, September 2021



Contents

List of Figures	xiii
List of Tables	xvii
1 Introduction	1
1.1 Introduction	1
1.2 Objective	2
1.3 Literature Survey	3
2 Theory	7
2.1 Wear modes	7
2.2 Single phase flow	9
2.3 Lagrangian multiphase modeling	12
2.4 Magnetism	14
2.5 Assumptions	16
3 Methods	17
3.1 Geometry	17
3.2 Single phase set-up	18
3.3 Physics models	19
3.4 Lagrangian multiphase set-up	19
3.5 Magnetic simulation set-up	21
4 Results	23
4.1 Plane selection	23
4.2 Mesh study	24
4.3 Single phase flow results	25
4.4 Temporal study	26
4.5 Particle sensitivity analysis	28
4.5.1 Particle source location	28
4.5.2 Particle size sensitivity	31
4.5.3 Particle shape sensitivity	34
4.5.4 Gear speed	35
4.6 Magnetic simulation	38
4.6.1 Test case	38
4.6.1.1 Remanent flux density	38
4.6.1.2 Magnetic susceptibility	40

4.6.1.3	Particle diameter	40
4.6.2	Gearbox model	42
4.6.2.1	Particle diameter	42
4.6.2.2	Gear speed	44
4.6.2.3	Magnet position	45
5	Conclusion	49
5.1	Conclusion	49
5.2	Future work	50
	Bibliography	51
A	Appendix 1	I

List of Figures

2.1	Magnet and magnetic field[23]	14
2.2	Classification of materials [26]	15
3.1	Gearbox geometry	17
3.2	Inside of a gearbox	17
3.3	Rotating and Non-rotating regions	18
3.4	Volume division	19
3.5	Magnet	21
3.6	Test case	21
4.1	Plane 1	23
4.2	Plane 2	23
4.3	Plane 3	23
4.4	Final mesh in plane 1	24
4.5	Method 1: Velocity vector (plane 1)	25
4.6	Method 2: Velocity vector (plane 1)	25
4.7	Method 3: Velocity vector (plane 1)	25
4.8	Method 1: Velocity vector (plane 1)	25
4.9	Method 2: Velocity vector (plane 2)	25
4.10	Method 3: Velocity vector (plane 3)	26
4.11	CFL contour of time step 0.002 sec	26
4.12	CFL contour of time step 0.004 sec	26
4.13	CFL contour of time step 0.008 sec	26
4.14	Injector positions	28
4.15	Particle distribution of injector 0	28
4.16	Particle distribution of injector 1	28
4.17	Particle distribution of injector 2	29
4.18	Particle distribution of injector 3	29
4.19	Particle distribution of injector 4	29
4.20	Particle distribution of multiple injector	29
4.21	Front view of particle distribution of injector 0	30
4.22	Front view of particle distribution of injector 1	30
4.23	Front view of particle distribution of injector 2	30
4.24	Front view of particle distribution of injector 3	30
4.25	Front view of particle distribution of injector 4	30
4.26	Front view of particle distribution of multiple injector	30
4.27	ISO view of particle distribution of multiple injector after 40secs	31

4.28	Top view of particle distribution of multiple injector after 40secs . . .	31
4.29	Side view of particle distribution of multiple injector after 40secs . . .	31
4.30	Particle mass distribution of particle size $6\mu\text{m}$	31
4.31	Particle mass distribution of particle size $14\mu\text{m}$	31
4.32	Particle mass distribution of particle size $6\text{-}14\mu\text{m}$	32
4.33	Particle mass distribution of particle size $14\text{-}20\mu\text{m}$	32
4.34	Front view of Particle mass distribution of particle size $6\mu\text{m}$ after 40secs	32
4.35	Front view of Particle mass distribution of particle size $14\mu\text{m}$ after 40secs	32
4.36	Front view of Particle mass distribution of particle size $6\text{-}14\mu\text{m}$ after 40secs	32
4.37	Front view of Particle mass distribution of particle size $14\text{-}20\mu\text{m}$ after 40secs	32
4.38	Particle mass distribution of shape factor 1	34
4.39	Particle mass distribution of shape factor 0.85	34
4.40	Particle mass distribution of shape factor 0.7	34
4.41	Front view Particle distribution of shape factor 1	35
4.42	Front view Particle distribution of shape factor 0.85	35
4.43	Front view Particle distribution of shape factor 0.7	35
4.44	Particle mass distribution of 2000RPM gear speed	35
4.45	Particle mass distribution of 1400RPM gear speed	35
4.46	Particle mass distribution of 0RPM gear speed	36
4.47	Particle velocity distribution of 2000RPM gear speed	36
4.48	Particle velocity distribution of 1400RPM gear speed	36
4.49	Particle velocity distribution of 0RPM gear speed	36
4.50	Remanent flux density: $2e^8\text{T}$	38
4.51	Remanent flux density: $3e^8\text{T}$	38
4.52	Remanent flux density: $4e^8\text{T}$	39
4.53	Remanent flux density: $5e^8\text{T}$	39
4.54	Magnetic field of the test case	39
4.55	$\chi=1$	40
4.56	$\chi=2$	40
4.57	$\chi=3$	40
4.58	$\chi=4$	40
4.59	Particle diameter of $6\mu\text{ m}$	40
4.60	Particle diameter of $10\mu\text{ m}$	40
4.61	Particle diameter of $14\mu\text{ m}$	41
4.62	Particle diameter of $6\text{-}14\mu\text{ m}$	41
4.63	Magnet position	42
4.64	Magnetic field	42
4.65	Particle mass distribution for $14\mu\text{m}$ particle diameter	42
4.66	Particle mass distribution for $6\text{-}14\mu\text{m}$ particle diameter	42
4.67	Particle velocity distribution of particle size $14\mu\text{ m}$	43
4.68	Particle velocity distribution of particle size of $6\text{-}14\mu\text{ m}$	43
4.69	Particle mass distribution of 2000RPM gear speed	44

4.70	Particle mass distribution of 1400RPM gear speed	44
4.71	Particle mass distribution of of 0RPM gear speed	44
4.72	Particle velocity distribution of 2000RPM gear speed	44
4.73	Particle velocity distribution of of 1400RPM gear speed	44
4.74	Particle velocity distribution of of 0RPM gear speed	45
4.75	Magnet position 1	45
4.76	Magnet position 1	45
4.77	Particle mass distribution of magnet position 1	46
4.78	Particle mass distribution of magnet position 2	46
4.79	Particle velocity distribution of magnet position 1	46
4.80	Particle velocity distribution of magnet position 2	46
4.81	Particle mass distribution of magnet position 1	46
4.82	Particle mass distribution of magnet position 2	46
4.83	Particle velocity distribution of magnet position 1	47
4.84	Particle velocity distribution of magnet position 2	47
A.1	Location of point for velocity and pressure plot	I
A.2	Pressure plot	I
A.3	velocity plot	I
A.4	Method 1: Velocity contour (plane 1)	II
A.5	Method 2: Velocity contour (plane 1)	II
A.6	Method 3: Velocity contour (plane 1)	II
A.7	Method 1: Velocity contour (plane 2)	II
A.8	Method 2: Velocity contour (plane 2)	II
A.9	Method 3: Velocity contour (plane 2)	II
A.10	Method 1: Velocity contour (plane 3)	III
A.11	Method 2: Velocity contour (plane 3)	III
A.12	Method 3: Velocity contour (plane 3)	III
A.13	Method 1: Tangential gear velocity	III
A.14	Method 2: Tangential gear velocity	III
A.15	Method 3: Tangential gear velocity	III
A.16	time vs total particle mass	IV
A.17	Particle distribution in each volume division	IV
A.18	ISO view of particle distribution of injector 0 at first time step	IV
A.19	ISO view of particle distribution of injector 1 at first time step	IV
A.20	ISO view of particle distribution of injector 2 at first time step	IV
A.21	ISO view of particle distribution of injector 3 at first time step	IV
A.22	ISO view of particle distribution of injector 4 at first time step	IV
A.23	ISO view of particle distribution of multiple injector at first time step	IV
A.24	Gear speed: 2000RPM	V
A.25	Gear speed: 1400RPM	V
A.26	Gear speed: 0RPM	V
A.27	Plot of comparison of particle count with different BC and particle diameters	V
A.28	Plot of comparison of particle count with gear speed	VI
A.29	Plot of comparison of particle count with magnet position	VI

A.30 Plot of comparison of particle count with magnet position (long time simulation) VII

List of Tables

3.1	Domain properties	18
4.1	Mesh properties	24
4.2	Drag force comparison between different particle sizes	33
4.3	Drag force comparison between different particle shapes	34
4.4	Base parameters	38
4.5	Capture efficiency	43
4.6	Capture efficiency of different gear speed	45
4.7	Capture efficiency of different magnet positions	47

1

Introduction

1.1 Introduction

A transmission gearbox changes the engine speed and torque of a mechanical system according to a variety of load conditions. The essential mechanical components in a transmission are the gears, bearings and shafts which are prone to damage and degradation due to friction during contacts. Gears are used to transmit the power from one shaft to another. The gear teeth and other moving parts such as bearings must be continuously separated by a thin film of lubricant so that the gearbox transmits power effectively with minimum losses. The lubricants prevent excessive wear and early failure of the gearbox. Nevertheless, wear in a gearbox is unavoidable. The friction between the gear teeth, during torque transmission, produces metal debris. If these metal debris are left unchecked in the system, it produces more debris and increase the rate of wear. The lubricant has to be changed more frequently to increase the lifespan of the gearbox.

Wear is defined as damage of solid surface caused by the relative motion between that surface and a contacting surface. These particles are typically in the micron range. The wear particles contained in the lubricating oil carry detailed information about the condition of the machine. Wear is influenced by contact geometry, length of exposure, environmental conditions, material properties, loading and sliding speed. From a macroscopic perspective, the wear debris produced from different wear processes appear as insignificant mass of particles that mostly look the same. However, on a microscopic level, the wear debris has a unique morphology and surface topography based on the type of wear mode. The study of morphology and topography of wear debris can be used to prevent the failure of the system and reduce wear. The different types of wear modes are described in section (2.1).

Computational Fluid Dynamics (CFD) simulations predict the lubricant flow, illustrating the oil supply to the main components of the gearbox. Thus CFD assesses the effectiveness of the lubrication system with respect to reliability. Different CFD methods which are implemented for gearbox simulation have been discussed in section (1.3).

Dip lubrication system is one of the most common types of lubrication system used in automotive transmission and is implemented in this work. In dip Lubrication the gears are partially immersed in oil. As the gears rotate, they transport the oil to

the meshing region. Although cooling will be enhanced for a large amount of oil, damaging effect of the oil increases which makes the torque transfer less efficient and there is an increase in drag on the rotating components of the system[1].

1.2 Objective

Wear in a mechanical system such as gearbox is unavoidable and if left unchecked, the wear debris produces more metal particles and increase the wear rate. One of the methods used in the Volvo gearbox is to place a magnet in the gearbox as a measure to ensure cleanliness of the lubricant. The magnet is intended to capture and retain the wear debris.

This study is conducted to investigate the possibility to combine fluid flow and magnet simulation in a commercial software (Star-CCM+) and provide additional information regarding the best placement of the magnet inside the dip lubricated oil sump to retain maximum number of metal particles and reduce the rate of wear.

1. Establish single phase oil flow.
2. Conduct particle sensitivity analysis and observe the particle distribution in the domain on the following parameters
 - a) Particle source location.
 - b) Particle size.
 - c) Particle shape.
3. Establish magnetic simulation.
4. Comparison study with different rotational speeds.
5. Different magnet placement in the gearbox

1.3 Literature Survey

The application of CFD to predict the flow inside a gearbox is challenging due to complexity of the domain which is bounded by the motion of the surface of the gears, shafts and bearings. Different modelling techniques have been proposed to apply CFD for gear motion and analyse different gearbox losses. Each technique differ in the accuracy of the results and simulation time. Franco Concli and Carlo Gorla[2] provided an overview of different numerical modelling approaches for gear motion and power losses and discussed their advantages, drawbacks and limitations. The authors discussed two main numerical approaches Smooth Particle Hydrodynamics (SPH) and Finite Volume (FV) methods coupled with different mesh handling techniques. The SPH method is applied by dividing the computational domain into a set of discrete elements or particles. Each particle represent a fixed amount of material in a Lagrangian reference frame. This method has low computational effort and low accuracy. The FV method discretize the domain into a set of cells and the system is governed by mass, momentum and energy equations on a control volume. This method is more accurate than the SPH method but introduces some mesh handling difficulties.

Marc C. Keller, Samuel Braun[3] investigated the SPH method further. A comparison of two dimensional setup of single-phase SPH to multiphase SPH simulation and the application of Volume Of Fluid (VOF) method is studied. The authors concluded that with the SPH method the computational effort can be tremendously reduced and this method could be used for simulations comprising of oil-gear interactions involving meshing gears.

Carlo Gorla, Franco Concli et al[4] investigated the FV method to predict the power loss. The simulations were performed for two different components, a disk and a gear. Additional simulations were performed to understand the influence of different parameters on the power loss. It was concluded that the error in the prediction for losses is less than 5 percent. Liu and Link et al[5] also studied the FV method to simulate oil supply, its distribution and power losses. It is also proved that the CFD method has been successfully developed to analyse injection-lubricated gearbox.

The different mesh handling techniques used in FV method for gear motion reviewed in paper[2] are sliding meshes, overlapping meshes, mesh morphing and remeshing. The authors concluded that the numerical methods are accurate and provide information about the oil distribution but are computationally expensive. FV method coupled with a suitable remeshing approach gives the most accurate results for power losses.

There are additional methods such as Moving Reference Frame (MRF) and Rigid Body Motion (RBM) which are being used in CFD. Franco Concli and Carlo Gorla[6] investigated the sliding mesh and MRF methods. The sliding mesh model is theoretically the most accurate method for simulating rotating motion and it can correctly describe the transient startup. This method is also computationally expensive. In this technique two cell zones are geometrically separated but numerically connected

by Arbitrary Mesh Interface (AMI). The MRF model is a steady state approximation in which individual cell zones rotate at different speeds. A local reference frame transformation is performed at the interface, to enable flow variables in one zone to be used to calculate fluxes at the boundary of the adjacent zones. The authors concluded that the sliding mesh approach describes the effect of unsteady fluctuations of the velocity and the MRF approach describes only steady state solutions. The MRF method is computationally less demanding. Both methods are in good agreement with the experimental values.

In the present work the numerical solution of the fluid domain inside the gearbox is performed with a finite volume method (FVM), which is based on the subdivision of the volume into cells and on the numerical solution of two governing equations, which represent the mass and momentum conservation. These two equations govern the behavior of a transient incompressible flow and must be enforced in each cell in which the computational domain is discretized. An attempt is made to implement the MRF method to develop the flow inside the gearbox.

Contaminants such as dirt, metal shards, soot etc in the lubricant can damage the gear and bearing surfaces, shorten the life of the equipment and cause breakdown. Different wear modes are studied to understand the wear morphology and topography from Wear particle Atlas[7], which is discussed further in section (2.1). It is found that a combination of rolling and sliding wear is most commonly found in gear systems. They have smooth surface with irregular shape.

Many research works have been carried out on magnetophoresis to separate magnetic particles especially in biotechnology to help manipulate and transport the particles. Miniaturization of magnetic separation has gained attention in recent years. It has the potential to offer a fast and efficient separation because the magnetic force on the particles is higher when the particles are closer to the magnet. Nicole Pamme and Andreas Manz[10] studied the magnetophoresis of magnetic particles and agglomerates in a continuous laminar flow. The authors demonstrated a technique for separating different magnetic particles from each other as well as from non magnetic materials. The separation of these particles were dependent on magnetic susceptibility, size of the particles, strength of the magnetic field and the flow rate. The bigger diameter particles with larger magnetic susceptibility were deflected more when compared to smaller diameter particles. Agglomerates of magnetic particles were deflected to a larger extent than single magnetic particles. At low flow rates, the magnetic force becomes too large and the deflection of magnetic particles increase. At even lower flow rates the particles would get stuck to the magnet.

Saud A. Khashan et al[11] used a one way coupled mixture model which reduces the computational cost with algebraic slip velocity to simulate the magnetophoresis in a 2D microfluidic system. The mixture models were considered as a substitute to Lagrangian Eulerian model due to the small stokes number of the flow. Saud A. Khashan and Edward P. Furlani[12] studied the magnetic separation and capture efficiency for a laminar flow through micro fluidic channel with a planar array of

soft embedded magnets. The total and local capture efficiency are analysed as a function of number of magnets, their volume, aspect ratio and spacing. The total and local capture efficiencies increase as the volume of the magnetic elements increases. It also increases as the element's aspect ratio increases and the element's spacing decreases.

Saud A. Khashan et al[13] implemented the fluid flow coupled with eulerian advection convection concentration equation to model the transport of the magnetic biospecies. The authors found that the axial magnetic forces plays an important role in vortex formation and increases the downward magnetic force experienced by the particles.

Jin-Woo Choi et al[14] designed and fabricated a bio-separator separating magnetic micro-beads from a carrier fluid. Antibody-coated magnetic beads have been separated from bio-buffer suspension solution. The magnetic characteristics have been numerically and experimentally studied to establish and validate the design and fabrication of the bio-separator.

Saud A. Khashan[15] investigated the effect of particle-fluid coupling on the transport and capture of magnetic particles in a microfluidic system under the influence of applied magnetic field. Particle motion takes into account dominant particle forces as well as two-way particle-fluid coupling. The analysis demonstrates that one-way coupling provides an overestimate of the magnetic force needed for the capture of magnetic particles. Two-way coupling provides a co-operative effect between the magnetic force and particle induced fluidic force that amplify the capture efficiency and provide accurate predictions.

Low intensity wet magnetic separators (LIMS) are used in the processing of iron ores for separating magnetic particles and non magnetic particles. Vasile Murariu[16] presented the results for LIMS incorporating DEM using ANSYS CFX for fluid flow and ANSYS EMAG for the simulation of the magnetic effects. Feiwang Wang et al[17] also studied the dynamic behavior of magnetic particles in LIMS. The authors developed a new approach in which particle tracing is employed to identify and determine particle trajectories through COMSOL multiphysics.

The use of different models in magnetophoresis mainly focus on microfluids and laminar flows. Some of these works have been studied to understand the setup and the influence of magnetic parameters to attract the magnetic particles (wear debris) on the magnet. Hence, this provides an initial understanding of the possibility to combine fluid flow and magnetic simulation in a turbulent gearbox model.

2

Theory

2.1 Wear modes

Wear and its characteristics is defined in section (1.1) and is further discussed in this section. The different types of wear modes and its surface topologies and morphologies are explained below[7].

1. Rubbing wear : During a normal break in of a surface, a unique layer is formed at the surface of the metal known as the 'shear mixed layer'. This layer may flow along the surface when subjected to stress, resulting in a very smooth wear track. Rubbing wear particles are generated because of normal sliding wear in a machine and results from peeling away of parts of the shear layer. The wear particles are platelet shaped and have a smooth surface ranging from $0.5\mu\text{m}$ to $15\mu\text{m}$ in size. Excessive quantities of contaminants such as sand in lubrication system can increase the rubbing wear generation. If the removal rate is increased to a point that the layer is removed faster than it is generated then the maximum particle size changes to $50\mu\text{m}$ or $200\mu\text{m}$ leading to severe sliding wear. Components with opposing surfaces of roughly same hardness are prone to such wear.

2. Cutting wear : This abnormal wear is produced when two surface penetrate one another. There are two ways of generating cutting wear. When a relatively hard component is misaligned or fractured, it results in a sharp edge penetrating the other softer surface. Particles generated in this method are coarse with $2\mu\text{m}$ - $5\mu\text{m}$ wide and $25\mu\text{m}$ - $100\mu\text{m}$ long. An alternative way to generate cutting wear is when hard abrasive particles either as contaminants or wear debris from another part of the system may be embedded on a soft surface. These particles penetrate the opposing surface. Particles generated in this method depend on the size of the abrasive particles embedded.

The particles generated are wire like with thickness around $0.25\mu\text{m}$. The presence of contaminants in the lubrication system does not generate cutting wear although the system wear rate increases.

3. Rolling Fatigue : Rolling fatigue particles are generated as a result of rolling bearing fatigue. There are 3 distinct types of particle associated with rolling fatigue spall particles, spherical particles and lamellar particles.

Spall particles constitute actual material removed as a pit or spall is formed. These particles are flat platelets with irregular shaped circumference and are typically in

the range of $100\mu\text{m}$.

The spherical particles are generated in the bearing fatigue cracks. These particles are generated even before the spalling occurs. Fatigue bearings generate several million spheres in the course of failure and are in the range of $1\mu\text{m}$ to $5\mu\text{m}$. Spherical particles are also generated due to cavitation erosion, welding and grinding process, lubrication oil also contains spherical contaminants.

Laminar particles are very thin in the range of $20\mu\text{m}$ to $50\mu\text{m}$. These particles are formed by passage of a wear particle through a rolling contact after adhering to a rolling element.

4. Combined rolling and sliding : This abnormal combination of wear modes is caused by fatigue and scuffing. They generate complex fusion of wear debris. Fatigue wear particles formed at the gear pitch line is similar to the particles generated during rolling fatigue. They have smooth surface with irregular shape. The chunkier particles are formed due to tensile stresses on the gear surface causing fatigue cracks to propagate deeper into the gear tooth.

Scuffing of gears are caused by too high loads or speeds. Excessive heat generation breaks down the lubricant film and causes adhesion of the mating gears. Scuffing usually affects each gear tooth and produces large amounts of wear debris. All particles have a rough surface and rugged circumference. Some of the large particles have striations on their surface indicating a sliding contact. Quantities of oxides are usually present and the degree of oxidation depends on the type of lubricant.

5. Severe Sliding wear : Severe sliding wear starts when the surface stresses become more due to excessive loads or speeds. The shear mixed layer becomes unstable and large particles break away and increases the rate of wear. If the stresses increase on the surface, a second transition point is reached where the complete surface breaks down. The particle size depends on stress level limit that is exceeded on the surface. Higher the stress level, higher is the particle size. Typically the particle size is greater than $15\mu\text{m}$. These particles have surface striations and are prominent as a result of severe sliding.

6. Adhesive wear : The wear is caused by localized bonding between contacting surfaces resulting in material transfer between the two surfaces. It takes place when materials slide against each other without any lubrication. They generate irregular particles.

7. Chemical/Corrosive wear : These particles are often too small to distinguish individually and is a result of improper fluid properties or heavy contamination.

Other than wear particles, particulate matter (contaminants) such as dust, asbestos, carbon flakes etc also exist if the oil is not filtered efficiently.

Conventionally, instruments such as analytical ferrography, spectrometric analysis etc are used to analyse the morphology and surface topography of the wear particles using techniques such as Microscopic analysis, magnetic flux, high heat vaporization

etc. These instruments capture information such as particle shape, composition, size distribution and concentration and determine the operating wear modes within the machines.

2.2 Single phase flow

Many textbooks describe the basic understanding of the fluid flow equations. The one described below is referenced from [9]

The governing equations of the fluid flow represents mathematical statements of conservation of mass, momentum and energy. The fluid behavior is described in terms of macroscopic properties such as velocity, pressure, density, temperature, their space and time derivatives. The fluid is regarded as a continuum whose properties are averaged over a large number of molecules. A fluid control volume is the smallest possible element of a fluid whose macroscopic properties are not influenced by individual molecules. Change in mass, momentum and energy of the fluid flow is accounted in the control volume due to fluid flow across its boundaries. The three governing equations are described below

The mass conservation law states that the mass of a fluid is conserved. The rate of increase of mass in a control volume is equal to the net rate of flow of mass into the control volume. The equation is given as

$$\frac{\partial(\rho)}{\partial t} + \frac{\partial(\rho u)}{\partial x} + \frac{\partial(\rho v)}{\partial y} + \frac{\partial(\rho w)}{\partial z} = 0 \quad (2.1)$$

$$\frac{\partial(\rho)}{\partial t} + \text{div}(\rho u) = 0 \quad (2.2)$$

Equation (2.1) is valid for unsteady, three dimensional compressible fluid flow and is called continuity equation. Equation (2.2) is a simplified version of the mass continuity equation. The first term on the left hand side is the rate of change of density with time and the second term is called the convective term describing the net mass flow out of the control volume.

The momentum conservation law states that the rate of change of momentum equals to the sum of the forces on a fluid particle. This law relates to the changes in the properties of a fluid particle. Each property of such a fluid particle is a function of the position (x,y,z) of the particle and time t.

The X momentum equation equation is given as

$$\rho \frac{Du}{Dt} = \frac{\partial(-p + \tau_{xx})}{\partial x} + \frac{\partial(\tau_{yx})}{\partial y} + \frac{\partial(\tau_{zx})}{\partial z} + S_{Mx} \quad (2.3)$$

The Y momentum equation equation is given as

$$\rho \frac{Dv}{Dt} = \frac{\partial(-p + \tau_{yy})}{\partial y} + \frac{\partial(\tau_{xy})}{\partial x} + \frac{\partial(\tau_{zy})}{\partial z} + S_{My} \quad (2.4)$$

The Z momentum equation is given as

$$\rho \frac{Dw}{Dt} = \frac{\partial(-p + \tau_{zz})}{\partial z} + \frac{\partial(\tau_{xz})}{\partial x} + \frac{\partial(\tau_{yz})}{\partial y} + S_{Mz} \quad (2.5)$$

The Equations (2.3)-(2.5) are called Navier-Stokes equations. The term on the left hand side describes the rate of increase of momentum per unit volume of a fluid particle. The first term on the right hand side accounts for a state of stress of a fluid particle. The second and third term in the right hand side gives the viscous stress in the respective direction. The last term is a source term which include contributions from body forces.

Different flow regimes are characterized based on Reynolds number defined as the ratio of inertial forces to viscous forces.

$$Re = \rho u L / \mu \quad (2.6)$$

Where u is the velocity, L is the characteristic length ρ is the density and μ is the dynamic viscosity of the fluid. At values below a critical Reynolds number, the flow is smooth and is called laminar flow. At values above a critical Reynolds number the flow behavior is random and chaotic. This regime is called turbulent flow.

Time dependent Navier-Stokes equations of fully turbulent flows are computationally expensive. Hence, the turbulent velocity is decomposed into mean and fluctuating velocities and the time averaged Navier-Stokes equations are obtained which provide adequate information about the statistics of turbulence. The time averaged Navier-Stokes equations is also called as Reynolds Averaged Navier Stokes (RANS) equations and are shown below.

$$\frac{\partial(\rho)}{\partial t} + div(\rho \bar{u}) = 0 \quad (2.7)$$

$$\frac{\partial(\rho \bar{u})}{\partial t} + div(\rho \bar{u} \bar{u}) = -\frac{\partial(P)}{\partial x} + div(\mu * grad(\bar{u})) + \left[-\frac{\partial(\overline{\rho u'^2})}{\partial x} - \frac{\partial(\overline{\rho u' v'})}{\partial y} - \frac{\partial(\overline{\rho u' w'})}{\partial z} \right] + S_{Mx} \quad (2.8)$$

$$\frac{\partial(\rho \bar{v})}{\partial t} + div(\rho \bar{v} \bar{u}) = -\frac{\partial(P)}{\partial y} + div(\mu * grad(\bar{v})) + \left[-\frac{\partial(\overline{\rho u' v'})}{\partial x} - \frac{\partial(\overline{\rho v'^2})}{\partial y} - \frac{\partial(\overline{\rho v' w'})}{\partial z} \right] + S_{My} \quad (2.9)$$

$$\frac{\partial(\rho \bar{w})}{\partial t} + div(\rho \bar{w} \bar{u}) = -\frac{\partial(P)}{\partial z} + div(\mu * grad(\bar{w})) + \left[-\frac{\partial(\overline{\rho u' w'})}{\partial x} - \frac{\partial(\overline{\rho v' w'})}{\partial y} - \frac{\partial(\overline{\rho w'^2})}{\partial z} \right] + S_{Mz} \quad (2.10)$$

When the instantaneous continuity and momentum equations are time averaged six additional unknowns (Reynolds stresses) are obtained. Hence these terms must be closed by additional turbulence models. Models such as the $k-\omega$ SST, $k-\epsilon$, etc are

used to close the unknown Reynolds stresses. The k- ϵ model is a well known and most commonly used turbulence model and is discussed in this section. The RANS equations and k- ϵ turbulence model is implemented in this thesis.

The k- ϵ model focuses on the mechanisms that affect the turbulent kinetic energy. The standard k- ϵ model has two model equations, one for k and one for ϵ . This model uses the transport equation for k and ϵ as given below

$$\frac{\partial(\rho k)}{\partial t} + \text{div}(\rho k U) = \text{div}\left[\frac{\mu_t}{\sigma_k} \text{grad}(k)\right] + 2\mu_t E_{ij} E_{ij} - \rho \epsilon \quad (2.11)$$

$$\frac{\partial(\rho \epsilon)}{\partial t} + \text{div}(\rho \epsilon U) = \text{div}\left[\frac{\mu_t}{\sigma_\epsilon} \text{grad}(\epsilon)\right] + C_{1\epsilon} \frac{\epsilon}{k} 2\mu_t E_{ij} E_{ij} - C_{2\epsilon} \rho \epsilon^2 / k \quad (2.12)$$

The equation contains five adjustable constants. The values are derived by comprehensive data fitting of a wide range of turbulent flows

$$C_\mu = 0.09$$

$$\sigma_k = 1$$

$$\sigma_\epsilon = 1.3$$

$$C_{1\epsilon} = 1.44$$

$$C_{2\epsilon} = 1.92$$

The Prandtl numbers σ_ϵ and σ_k connect the diffusivities of k and ϵ to eddy viscosity μ_t . The modelled equation for ϵ assumes that its production and destruction terms are proportional to the production and destruction terms of the k equation. ϵ increases rapidly as k increases rapidly and decreases fast to avoid negative values of k. To model the Reynolds stresses with the k- ϵ Boussinesq relation is used

$$-\rho \overline{u'_i u'_j} = \mu_t \left[\frac{\partial U_i}{\partial x_j} + \frac{\partial U_j}{\partial x_i} \right] - \frac{2}{3} \rho k \delta_{ij} = 2\mu_t E_{ij} - \frac{2}{3} \rho k \delta_{ij} \quad (2.13)$$

Turbulent flows are characterized by a complicated boundary layer. y^+ is an analytical profile covering different regimes near the wall. The boundary layer thickness is divided into inner and outer regions. The inner region is further divided into a viscous layer ($0 < y^+ < 5$), a buffer layer ($5 < y^+ < 30$) and a fully turbulent layer ($30 < y^+ < 400$). The wall y^+ is a dimensionless number given as

$$y^+ = \frac{y u^*}{\nu} \quad (2.14)$$

$$u^* = \sqrt{\frac{\tau_w}{\rho}} \quad (2.15)$$

Where u^* is the wall friction velocity, y is the distance of the centroid of a cell from the wall and ν is the kinematic viscosity.

The wall y^+ should essentially be around 30 or more so that the entire laminar upto log law region is entirely modeled and turbulent zone is considered as well in the first prism layer near the walls in a fluid flow.

2.3 Lagrangian multiphase modeling

Multiphase flow is defined as the simultaneous presence of different phases (solid, gas and liquid) in a domain of interest. There are different multiphase flows such as gas/solid, gas/liquid and liquid/solid flows. Multiphase flows are very complex as it involves movement of many individual particles and their interaction with the fluid flow. It becomes more complex when phase change is involved in the flow.

The flow is considered dilute if the particle volume fraction is in the range of 10^{-6} to 10^{-3} . The particle motion is influenced by the carrier phase and visa versa (Two-way coupling). If the volume fraction is below 10^{-6} then the particle motion does not influence the carrier phase (One-way coupling). A dense flow consists of volume fraction greater than 10^{-3} [18, 19,20].

One of the methods to solve two-phase flow is by implementing the Eulerian-Lagrangian approach (E-L) which treats the fluid as a continuum and particles as a discrete entities. This approach is advantageous when compared to Eulerian-Eulerian approach (E-E) as it provides more detailed information on the discrete particle behavior. It is assumed that the Lagrangian property associated with a particle at a point is same as the Eulerian property evaluated at that point. E-L approach divide the solution into two steps. The Navier Stokes equation solves the transport equation for the carrier phase and the Lagrangian equations solve the particle model [21]. The algorithm alternates between the two steps until a convergence is reached. Both the equations are inter-related by source terms.

The first task of Lagrangian multiphase approach is to calculate the particle motion in a Lagrangian frame of reference. All the relevant forces such as drag, lift, added mass, body force etc have to be taken into account when calculating the particle trajectories. The second task is to calculate the fluid flow in the Eulerian frame of reference by using different turbulence models (LES, RANS etc).

Additional processes such turbulent dispersion, particle-wall interactions, particle-particle interactions have to be considered based on the different strategies used to solve the fluid flow.

$$m_p \frac{du_p}{dt} = \oint_s \sigma_{ij} n_j ds + m_p g = \sum F_i \quad (2.16)$$

Equation (2.16) represents the translational motion of individual particles[22]. The first term on the right hand side is the stress tensor and the second term is the body force. All the relevant forces mentioned above arise from the stress tensor except the body force. Each force is modelled in E-L approach. The influence of the carrier phase is taken into account by the velocity of the fluid (v) in equation (2.18).

The forces considered in this thesis are gravity, drag force and magnetic force. The drag force is given in equation (2.17)[8].

$$F_d = \frac{1}{2} C_d \rho A_p |v_s| v_s \quad (2.17)$$

$$v_s = v - v_p \quad (2.18)$$

C_d is the drag coefficient of the particle.

ρ is the density of the continuous phase.

v_s is the particle slip velocity.

v_p is the instantaneous particle velocity

v is the instantaneous velocity of the continuous phase.

A_p is the projected particle area

The drag coefficient C_d is a function of small scale flow features around the particle which is impractical to resolve spatially. Hence the drag coefficient is obtained by correlations. Two correlations have considered in this thesis (Schiller- Naumann and Haider Levenspiel).

The Schiller-Naumann correlation is suitable for solid spherical particles[8]

$$C_d = \frac{24}{Re_p}(1 + 0.15Re_p^{0.687}) \quad Re_p \leq 10^3 \quad (2.19)$$

$$= 0.44 \quad Re_p > 10^3$$

$$Re_p = \frac{\rho v_s D_p}{\mu} \quad (2.20)$$

The Haider and Levenspiel correlation is suitable for particles of different shape [8]

$$C_d = \frac{24}{Re_p}(1 + ARe_p^B) + \frac{C}{1 + \frac{D}{Re_p}} \quad (2.21)$$

$$A = 8.1716e^{-4.0665\phi}$$

$$B = 0.0964 + 0.5565\phi$$

$$C = 73.690e^{-5.0746\phi}$$

$$D = 5.3780e^{6.2122\phi}$$

A shape factor provides a single parameter user input to change the drag calculation and consider the change in particle shape. It is a function of particle Reynolds number and particle sphericity. Sphericity is defined as the ratio of surface area of a sphere having the same volume as the actual particle to the actual surface area of the particle. Smaller sphericities represent flat disc while a sphericity of 1 represents a perfect sphere. Haider and Levenspiel drag model is coupled with the shape factor. The change in shape is accounted internally by the change in the drag force[8].

Both the drag force and the gravity force are integrated in equation (2.16) to give the trajectories of the individual particles.

If the number of particles in the domain is small, then each individual particle can be tracked and solved for using the particle equation of motion. But if the number of particles is very large, it becomes too expensive to track all the individual particles. Hence, a parcel representing a collection of real particles are used to save computational time and cost. The numerical results are accurate when large number of parcels are present but it also leads to high computational cost. All particles inside a parcel are assumed to be spherical and have identical properties.

2.4 Magnetism

This section describes basic understanding of different magnetic properties before implementing them in the magnetic simulation.

Magnetism refers to the phenomena arising from the forces caused by the magnets. The motion of electrically charged particles gives rise to magnetism. All materials experience magnetism, some more strongly than the others. A magnetic field or magnetic field strength (H) is the magnetic force exerted by the magnet. The strength of the magnetic field is represented by imaginary lines called the magnetic lines of force as shown in 2.2. The closer together the magnetic lines are, the stronger is the magnetic field and magnetic force. Magnetic fields are generated by rotating electric charges having angular momentum or spins. Most of the electric charges form pairs whose spins are in opposite directions and cancel each other out. However, some atoms contain one or more unpaired charges whose spin produces a directional magnetic field. When a significant majority of unpaired charges are aligned with spins in the same direction, they produce macroscopic magnetic field[24]. The alignment of the electric charges are produced by an external magnetic field. If the alignment of electric charges exist even after the removal of external magnetic field or current, then it is known as permanent magnet.

Remanent flux density (B_r) is the residual magnetization left after the external magnetic field is removed. Hence remanent flux density is a measure of quality of a permanent magnet.

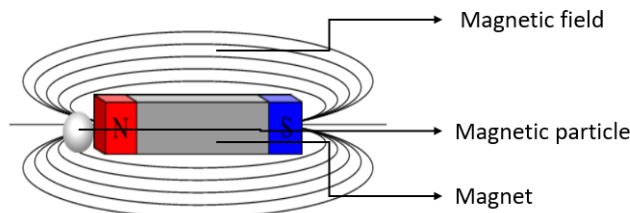


Figure 2.1: Magnet and magnetic field[23]

The direction of magnetic lines propagate outward from the north pole of the magnet and enter through the south pole. The strength of the magnetic field varies with location and is the strongest very close to the magnet.

Magnetic flux density (B) is the amount of magnetic force induced on a particle placed in the magnetic field. Both magnetic field (H) and magnetic flux density (B) are related by magnetic permeability (μ) [25]

$$B = \mu_0 \mu_r H \quad (2.22)$$

μ_0 = Permeability of free space = $4\pi \cdot 10^{-7}$

μ_r = Permeability of the material

Magnetic permeability (degree of magnetization) is defined as the ability of a material to support the formation of magnetic field. For non-magnetic materials such as air μ_r is equal to 1.

Magnetic susceptibility (χ) is defined as the ability of a material to be attracted or repelled in a magnetic field.

$$\chi = M/H \quad (2.23)$$

M is the magnetization. Materials where magnetic moments of each atom can be made to align in one particular direction are said to be magnetizable and the extent to which the materials are magnetized is called as magnetization. Magnetic properties such as susceptibility and magnetization is usually measured through experiments such as Vibrating Sample Magnetometer (VSM) by plotting magnetization graph or B-H curve.

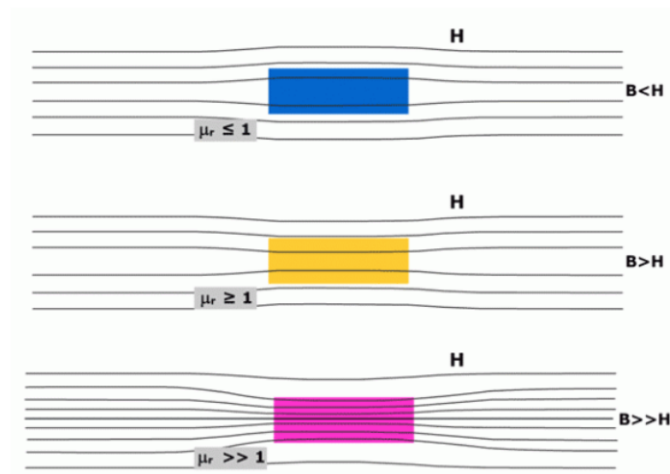


Figure 1: Magnetic Permeability in Different Materials

Figure 2.2: Classification of materials [26]

Materials are classified based on their magnetic permeability and susceptibility (diamagnetic, paramagnetic and ferrromagnetic).

Diamagnetic material : The relative magnetic permeability is less than 1 and susceptibility is less than 0. These materials do not attract to an external magnetic field.

Paramagnetic material : The relative magnetic permeability is slightly greater than 1 and the susceptibility is slightly greater than 0. These materials are slightly attracted to an external magnetic field.

Ferromagnetic material : The relative magnetic permeability is very high. These materials are strongly attracted to an external magnetic field.

The magnetic force is implemented in the equation of particle motion in equation (2.16) along with drag and gravity forces. The magnetic force is given by [14]

$$F_{mag} = \chi V_p B(\nabla H) \quad (2.24)$$

V_p is the volume of the particle.

From equation (2.24), it is evident that larger particles experience greater magnetic force and are more strongly attracted to the magnet.

The attraction of particles on the magnet is analysed in terms of capture efficiency. Total capture efficiency is defined as the ratio of number of particles deposited on the magnet to the total number of particles in the domain. Local capture efficiency is defined as the ratio of number of particles deposited on the magnet to the number of particles present in the volume division in which the magnet is present. The volume division will be discussed in section (3.4).

2.5 Assumptions

Some assumptions are made in order to simplify the problem description.

1. The model is cut so that only the part below the oil surface is considered
2. One way coupling is assumed as the wear particles are small and dilute in the carrier phase.
3. Constant Temperature in the domain.
4. Constant density for both particle and fluid phase.
5. Particle material is assumed to be stainless steel
6. Lagrangian Particle Tracking (LPT) modelling approach is used as there is no particle-particle and particle wall interactions.
7. Simple particle shapes are taken into account as complex shape of real wear particle debris cannot be modelled in LPT.

3

Methods

Star-CCM+ is a commercial CFD solver, part of Siemens Simcenter portfolio. This software is capable of solving multi-disciplinary problems in fluid and solid continuum mechanics. The software also includes an integrated mesher. The geometry which is already prepared in ANSA is imported into Star-CCM+ where the geometry is meshed and simulation is carried out.

3.1 Geometry

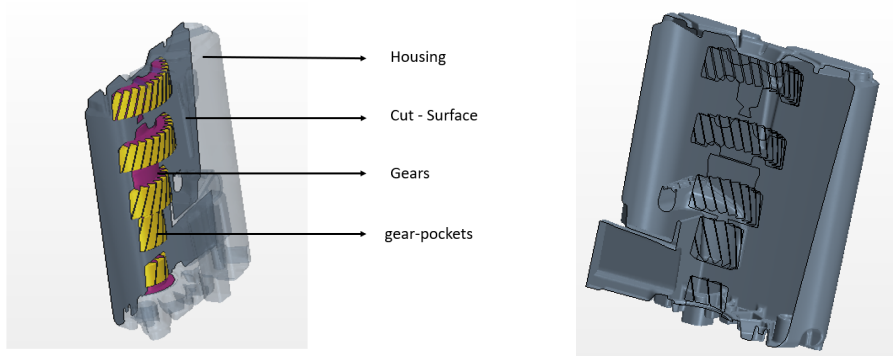


Figure 3.1: Gearbox geometry **Figure 3.2:** Inside of a gearbox

Figure (3.1) and figure (3.2) shows the geometry of the gearbox which is directly imported from ANSA into star-CCM+. Only cross section of the geometry is considered for the analysis. The gearbox consists of the gearbox housing, gears, gear-pockets and cut-surface. These four components also make up the boundary conditions of the domain. All the surfaces are modeled with no-slip wall boundary condition except for the gear-pockets and the cut-surface which are modeled with slip wall condition. All the gears have different size and the cross-section of the gearbox considered is not cut symmetrically. The inside of the gearbox has geometrical complexities which influence the flow inside the gearbox.

Table 3.1: Domain properties

Axis of rotation	[0,-160.025,-122.35]
Rotation speed	2000 RPM
Rotation direction	[0,0,1]
Oil density	815 kg/m ³
Domain volume	0.01 m ³

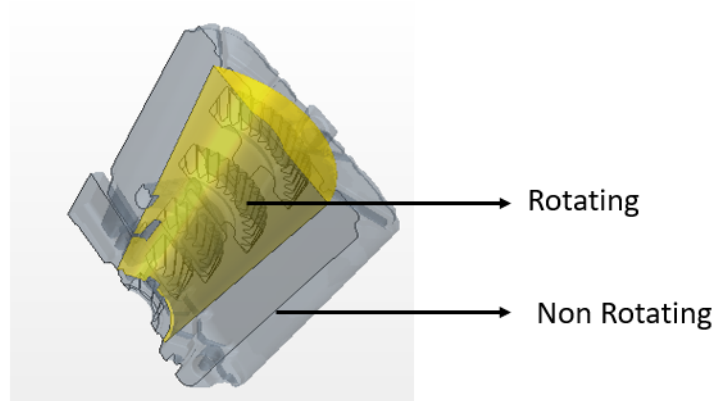
3.2 Single phase set-up

The single phase oil behavior is analysed by setting the gear into rotational motion. Three different methods namely are compared to set rotational motion of the gears.

1. Tangential velocity specification
2. Moving reference frame (MRF) with single region
3. Moving reference frame (MRF) with two regions

Tangential velocity specification is one of the simplest methods to set rotational motion. In this method 'Lab reference frame' is established for the region and only the gear boundary is set to tangential velocity with the specified axis of rotation and rotation speed.

The MRF method has been described in section (1.3). MRF with single region method is implemented by creating a new 'rotating frame of reference' with specified axis of rotation and rotation speed. This frame of reference is established for entire region. In this method the whole oil domain is rotating while the gearbox housing is stationary (Lab Reference frame).

**Figure 3.3:** Rotating and Non-rotating regions

MRF with two regions consists of a rotating and non rotating regions as shown in figure (3.3). The rotating region consists of the gears and gear-pockets and the non-rotating region consists of the gearbox housing and part of the cut-surface. A new 'rotating frame of reference' is established in the rotating region and 'lab frame' is

established in the non-rotating region.

A comparison of results is made between the three methods in section (4.3) and the best method for simulating rotating motion of the given geometry is discussed.

3.3 Physics models

The physics models enabled in developing single phase flow is discussed in this section. A segregated solver is chosen as it works well with in-compressible flows and needs less computational resources[28].

The realizable $k-\epsilon$ model is implemented as the turbulence model with two layer wall treatment function. This model is the most proven and widely used in simulations involving rotation and recirculation.

3.4 Lagrangian multiphase set-up

The material of the wear particles are assumed to be stainless steel. One way coupling is assumed, as the wear debris are quite small, dilute and they do not affect the fluid motion. Hence Lagrangian particle tracking is used to introduce the particles in the domain.

Drag force, gravity and magnetic forces are considered to be the dominant forces acting on the particles. Schiller Naumann drag coefficient model is used for spherical particles and Haider-Levenspiel drag coefficient model is used for non spherical particles in combination with a user shape factor to account for different shapes. Turbulent dispersion is enabled to synthesize the fluctuating nature of the turbulent velocity field in the fluid phase. The turbulent dispersion collaborates with the RANS turbulence model. The particles have wall boundary with rebound interaction mode. The particles are injected from a point injector.

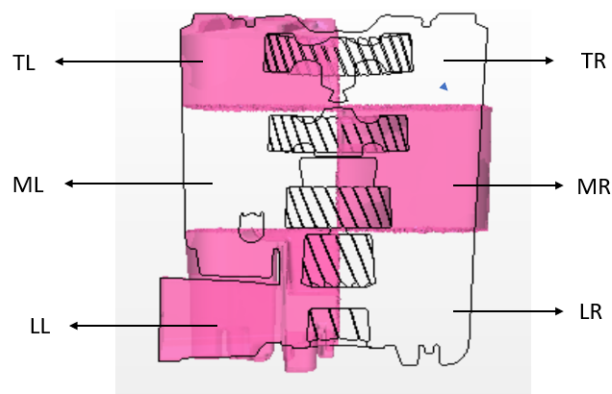


Figure 3.4: Volume division

3. Methods

Figure (3.4) shows that the whole domain is divided into 6 volumes to study the particle accumulation in each volume division. All the results related to particle sensitivity and magnetism are discussed with respect to the particle distribution in each of these volume divisions.

TL - Top-Left division
 TR - Top-Right division
 ML - Middle-Left division
 MR - Middle-Right division
 LL - Last-Left division
 LR - Last-right division

3.5 Magnetic simulation set-up

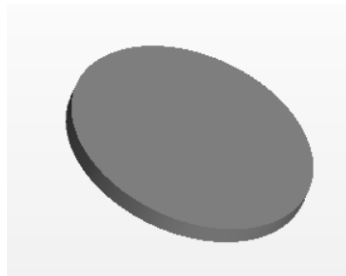


Figure 3.5: Magnet

The magnet is circular disc of 42mm diameter and 6mm thick. The magnet surfaces have stick boundary condition. The magnetic properties of the material is given below

$$B_r = 0.3\text{T}$$

$$\mu_r = 1.02$$

$$\mu = 1.2e^{-6}$$

Two regions and physics models are created in the domain. Solid region is assigned to the magnet and fluid region is assigned to the rest of the gearbox. Electromagnetism and finite volume magnetic vector potential is enabled for both the physics models to consider the magnetic effects. Anti-symmetric perfectly electric conductor boundary condition is used on the magnet to prevent any magnetic flux from crossing the boundary.

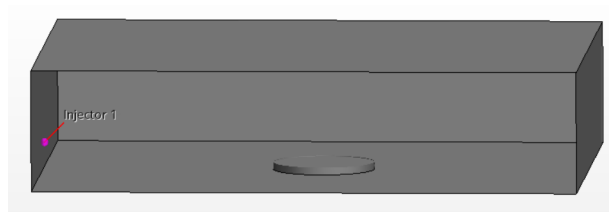


Figure 3.6: Test case

The flow inside the gearbox is turbulent and Since the magnet surface has stick boundary condition, it is difficult to understand if the particles are deposited on the magnet by the influence of magnetic force or just by the influence of the flow. Hence, the magnetic simulation is initially implemented on a test case before applying it

3. Methods

on the gearbox model. The test case has the same dimensions of the gearbox and laminar flow is assumed for the sake of simplicity. Figure 3.6 shows the geometry of the test case.

4

Results

4.1 Plane selection

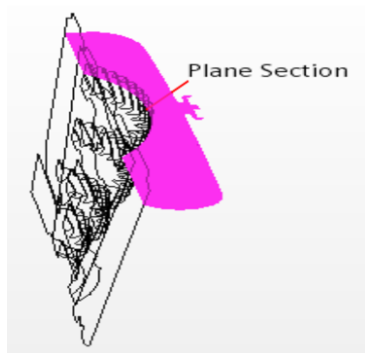


Figure 4.1: Plane 1

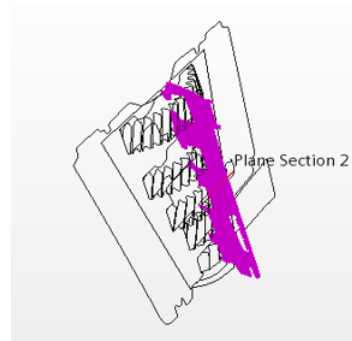


Figure 4.2: Plane 2

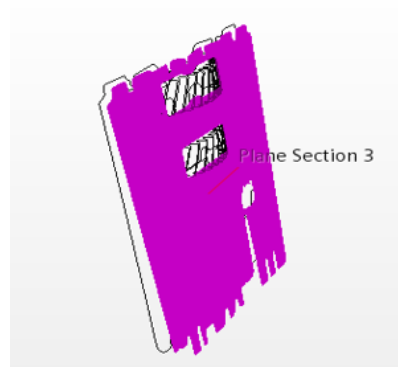


Figure 4.3: Plane 3

Three different planes are created to analyse the fluid behavior in the domain. Figure (4.1) shows plane 1 created in X-Y plane near the middle region of the biggest gear. Figure (4.2) shows plane 2 created in Z-Y plane in the middle of the gearbox. Figure (4.3) shows plane 3 created in X-Z plane close to the cut-surface of the gearbox.

4.2 Mesh study

The mesh study is conducted with 3 different mesh sizes. A comparison of different mesh sizes is done by plotting velocity and pressure data for a single point in the domain. Figure (A.1) in appendix shows the location of the point where the velocity and pressure data is extracted. Figure (A.2) and figure (A.3) in appendix shows the pressure and velocity plots of different mesh size. The fluctuations in both the figures do not stabilize due to turbulence but the fluctuations follow similar pattern periodically. The final mesh configuration is given in table 4.1.

Table 4.1: Mesh properties

Base size	4mm
Minimum surface size	1mm
Number of prism layer	2
Prism layer thickness	3.5mm
Total number of cells	0.9 million
Gear surface target size	3mm

The final mesh is chosen such that it reduces the computational time. The number of prism layers is restricted to 2 to achieve adequate wall y^+ value to consider turbulence effects near the wall. The final mesh is shown in figure (4.4). Even though the flow solution accuracy is compromised by choosing a coarser mesh, the overall solution is improved as it reduces the mass loading from the lagrangian phase.

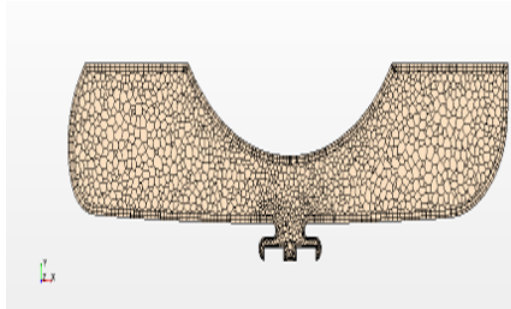


Figure 4.4: Final mesh in plane 1

4.3 Single phase flow results

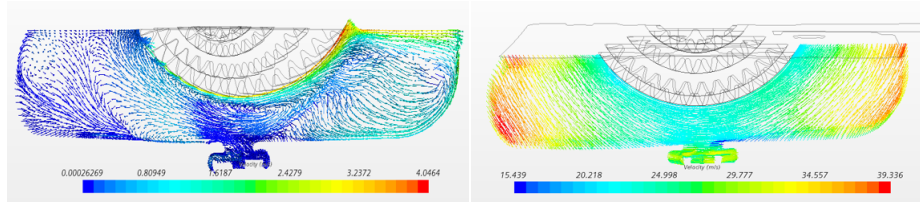


Figure 4.5: Method 1: Velocity vector (plane 1) **Figure 4.6:** Method 2: Velocity vector (plane 1)

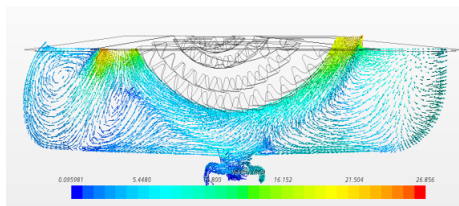


Figure 4.7: Method 3: Velocity vector (plane 1)

Figure (4.5, 4.6, 4.7) compare the velocity vectors for all the three methods in plane 1. Figure (A.4) - (A.12) in appendix compares the scalar velocity contours of the three methods in different planes. All the three methods have similar tangential velocity on the gear surface as shown in figure (A.13)-(A.15) in appendix. Method 1 captures the turbulent effect and re-circulation quite well in the domain. Method 2 is an extreme case where the velocity contours are very high in the domain as it considers the whole region to be rotating with the same rotation speed. Hence all the vectors are directed in the direction of rotation. Method 3 captures the turbulence effect better than method 2 but the gradients at the interface of rotating and non-rotating regions are very high. This is because, the geometry is not symmetric and the gears are not similar in size.

MRF method (method 2 and method 3) is not an appropriate method to be implemented in this study. Hence Tangential velocity (method 1) is used to develop the fluid flow in the domain. Method 1 is a robust method which is desirable when there is complexity in the geometry and in addition, particles and magnetism is to be included in the oil flow simulation of the gearbox.

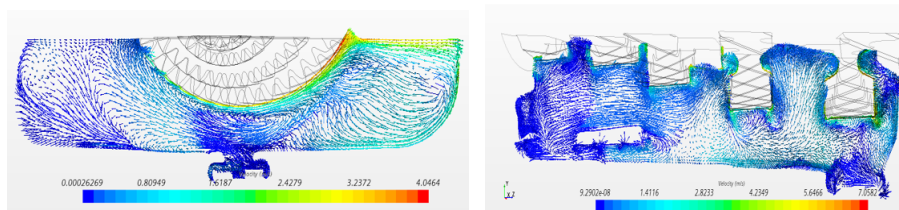


Figure 4.8: Method 1: Velocity vector (plane 1) **Figure 4.9:** Method 2: Velocity vector (plane 2)

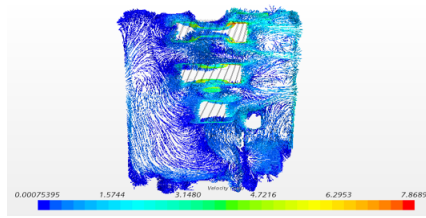


Figure 4.10: Method 3: Velocity vector (plane 3)

Figure (4.8) - (4.10) shows the velocity vectors in different planes. Figure (4.9) shows that the velocity is higher close to the gear when compared to walls. Figure (4.10) shows that the right part of the domain has higher velocity and turbulence due to complex internal geometry. There are strong re-circulation regions in the right part of the domain.

4.4 Temporal study

Obtaining a CFD solution is an iterative process. Temporal study is conducted to achieve a solution which does not change with time. Single phase oil flow is developed using steady state and is run until periodic fluctuations are attained (12000 iterations). Unsteady simulation is carried out to introduce particles in the flow. The flow is run for 1s before introducing the particles.

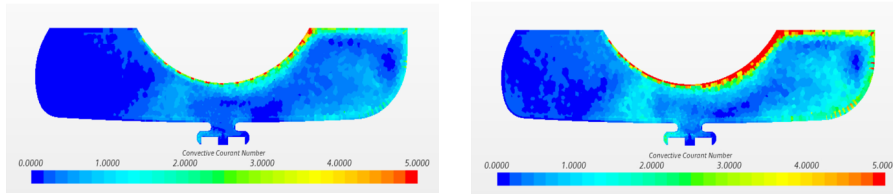


Figure 4.11: CFL contour of time step 0.002 sec

Figure 4.12: CFL contour of time step 0.004 sec

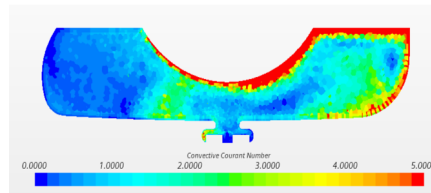


Figure 4.13: CFL contour of time step 0.008 sec

Temporal study is conducted based on the average CFL number. Figure (4.11)-(4.13) shows the CFL contour in plane 1. An average CFL number less than the minimum cell size is considered to give accurate temporal results (CFL number less than 1 at the minimum cell size of 1mm). Time step size of 0.002s has an average CFL number of 0.44. But the computational time required to simulate is very high. Hence coarser time steps are studied to reduce the computational time. The time

step 0.004s has an average CFL number of 0.89 and time step of 0.008s has an average CFL number of 1.78. Although 0.008s is a coarser time step, it provides accurate results closer to the results of time step size of 0.002. Figure (A.16) in appendix show a comparison of all the three time steps with less than 5% loss of total particle mass in the domain. Hence time step size of 0.008s is used for all the simulations. Figure (A.17) shows a simulation is run for 80s and the particle distribution in each of the volume division shown in figure (3.4) gets stabilized after 40s. Hence all the simulations are run for 40s.

4.5 Particle sensitivity analysis

The particle sensitivity analysis consists of comparison of particle distribution for different sensitivity parameters (particle source injections, particle sizes, particle shapes and gear speed). All the simulations is run for 40 secs with a time step size of 0.008sec and total number of cells in the domain is 0.9 million.

4.5.1 Particle source location

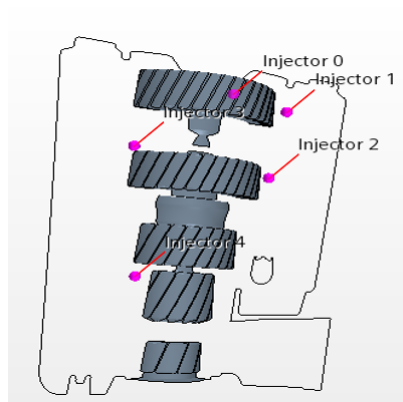


Figure 4.14: Injector positions

For analysis of particle source injection, 6 different simulations are conducted by injecting 1000 parcels in the first time step. There are 5 different injection positions as shown in figure 4.14. Injector position 0,1 and 2 is located in high velocity region and injector 3 and 4 is located in low velocity regions. The final simulation injects equal number of particles (20% of total number of particles) in each of the 5 injector positions. Mono-dispersed particle size of $14\mu\text{m}$ is assumed to be injected into the domain.

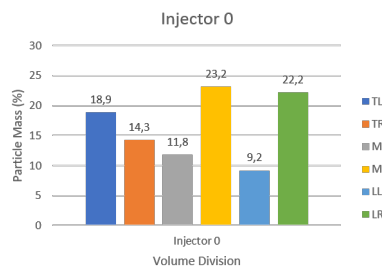


Figure 4.15: Particle distribu-
tion of injector 0

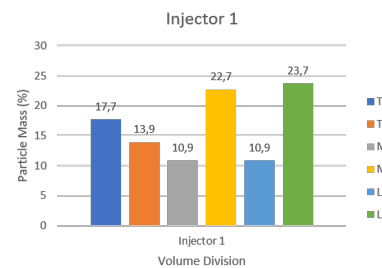


Figure 4.16: Particle distribu-
tion of injector 1

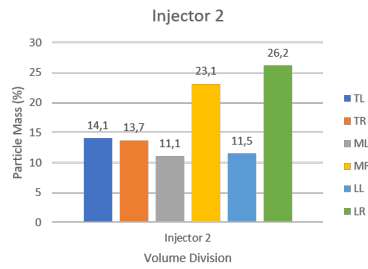


Figure 4.17: Particle distribution of injector 2



Figure 4.18: Particle distribution of injector 3

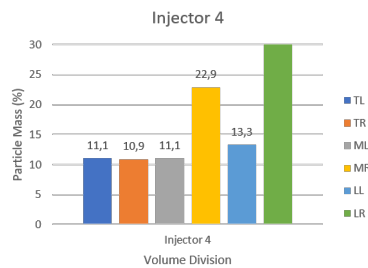


Figure 4.19: Particle distribution of injector 4

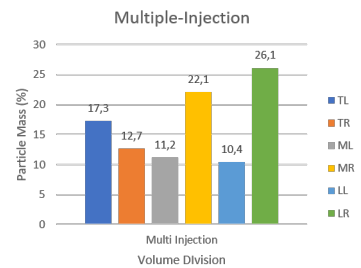


Figure 4.20: Particle distribution of multiple injector

Figures (4.15)-(4.19) show bar graphs of particle mass distribution in each of the volume division for different injector positions shown in figure (3.4). Each bar in a single graph represents a single volume division. All the graphs follow the same trend. The percentage of particle mass is dominant in MR and LR volume divisions irrespective of where the particles are injected. The mass percentage of particle distribution is less affected by injector position. The mass percentage of particle distribution of TL volume division in injector 0 and injector 1 are slightly greater than other 3 injectors and the mass percentage of particle distribution of LR volume division in injector 2,3 and 4 is slightly greater than injector 0 and 1 due to the injector positions. The particle trajectories are highly influenced by the fluid flow and settles in the same regions irrespective of where the particles are injected. Particle mass accumulation is less in LL volume division in all the cases due to complex internal geometry and higher velocities in that region. The particle mass distribution in the gearbox is less affected by the particle source location.

Figure (4.20) shows particle mass distribution of a more realistic case in which particles are injected in multiple injectors simultaneously with equal number of particles (20% of total number of particles) in all the 5 injector positions. The particle mass distribution follow the same trend as before and observe that MR and LR volume divisions have more particle mass when compared to other divisions. Since multiple injection is a more realistic case as we do not know where the particles are injected in the domain, multiple injectors are used for other particle sensitivity analysis.

4. Results

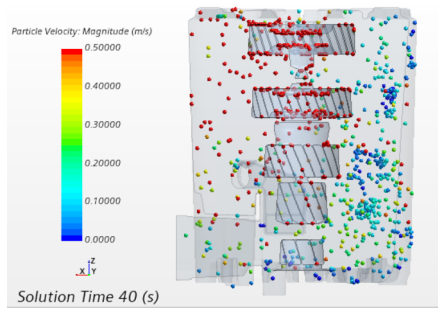


Figure 4.21: Front view of particle distribution of injector 0

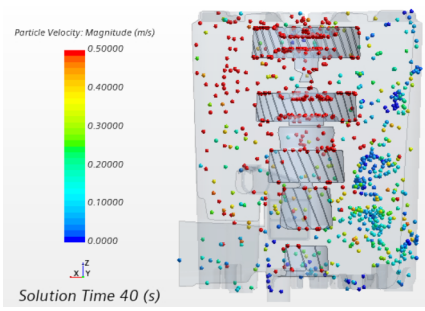


Figure 4.22: Front view of particle distribution of injector 1

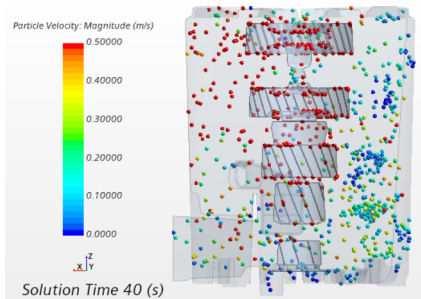


Figure 4.23: Front view of particle distribution of injector 2

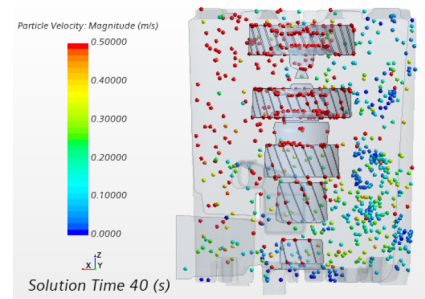


Figure 4.24: Front view of particle distribution of injector 3

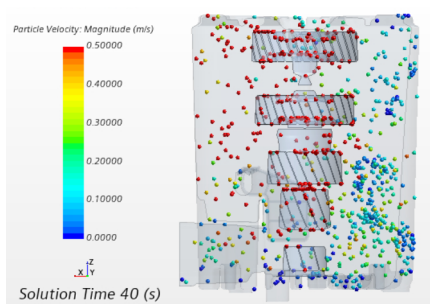


Figure 4.25: Front view of particle distribution of injector 4

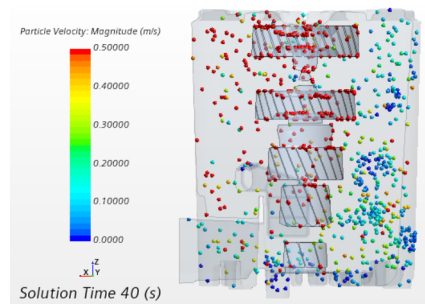


Figure 4.26: Front view of particle distribution of multiple injector

Figure (A.18)-(A.23) in appendix show the particles injected in the first time step for different injector positions. Figure (4.21)-(4.26) Shows the final particle velocity distribution in the domain after 40 secs. The velocity of the particles is more close to the gears because the fluid velocity is higher near the gears when compared to the walls.

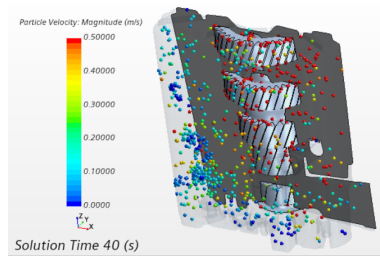


Figure 4.27: ISO view of particle distribution of multiple injector after 40secs

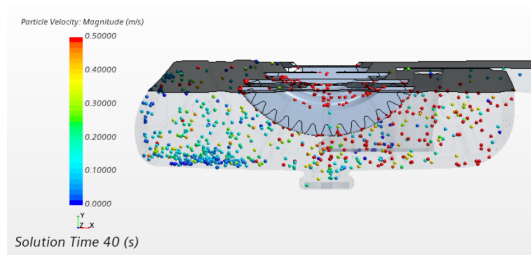


Figure 4.28: Top view of particle distribution of multiple injector after 40secs

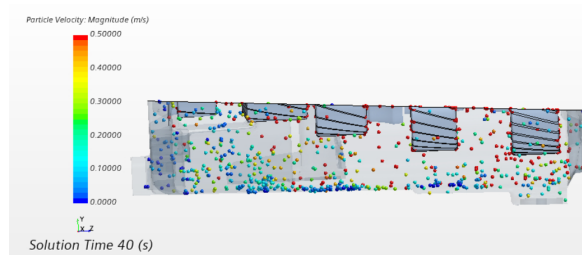


Figure 4.29: Side view of particle distribution of multiple injector after 40secs

Figure (4.27)-(4.29) show particle distribution of multiple injectors after 40secs in different geometric views. Most of the particles settle down in the casing in the low velocity regions of the domain due to particle forces and has lower particle velocity. The right part of the domain has higher fluid velocity due to complex internal geometry and hence the particle velocity is also higher in the right part of the domain as seen in figure(4.28).

4.5.2 Particle size sensitivity

Four different simulations are conducted for particle size sensitivity. 2 simulations include mono-dispersed particle size of $6\mu\text{m}$ and $14\mu\text{m}$. The last two simulations include a normal distribution of particle size ranging from $6\text{-}14\mu\text{m}$ and another normal distribution of particle size ranging from $14\text{-}20\mu\text{m}$. Particle size larger than $20\mu\text{m}$ is not considered as the filter efficiency is higher for larger particles and can be captured by the filter effectively.

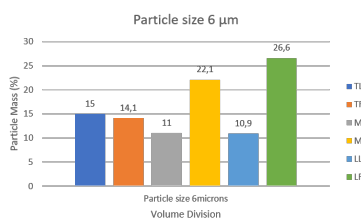


Figure 4.30: Particle mass distribution of particle size $6\mu\text{m}$

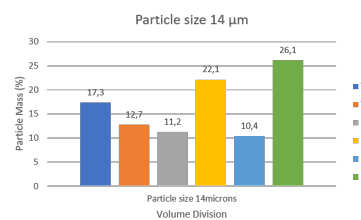


Figure 4.31: Particle mass distribution of particle size $14\mu\text{m}$

4. Results

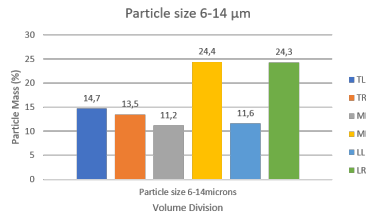


Figure 4.32: Particle mass distribution of particle size 6-14 μm

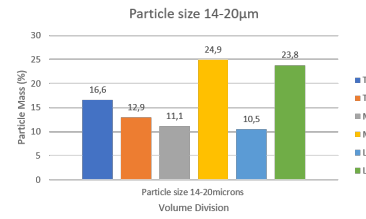


Figure 4.33: Particle mass distribution of particle size 14-20 μm

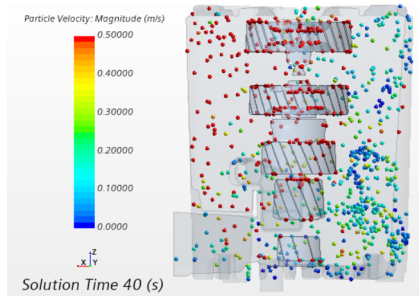


Figure 4.34: Front view of Particle mass distribution of particle size 6 μm after 40secs

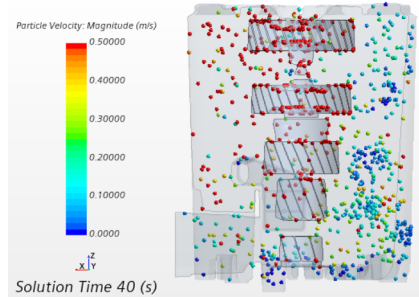


Figure 4.35: Front view of Particle mass distribution of particle size 14 μm after 40secs

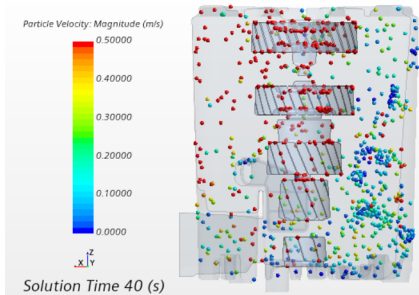


Figure 4.36: Front view of Particle mass distribution of particle size 6-14 μm after 40secs

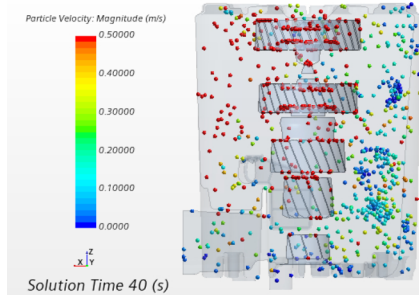


Figure 4.37: Front view of Particle mass distribution of particle size 14-20 μm after 40secs

Figure (4.30)-(4.33) show comparison of particle mass distribution between different particle sizes in each of the volume division. Increasing the particle size, increases the particle mass and drag force experienced by the particle. This force is still not high enough to overcome the dominance of the carrier phase and change the particle trajectories. Hence, all the four graphs show similar trend where particle mass is accumulated more in MR and LR volume divisions.

In figure (4.30), figure (4.34) and figure (4.31), figure (4.35), two different mono-dispersed particles are compared. Table (4.2) shows that drag forces increases with increase in particle size.

Table 4.2: Drag force comparison between different particle sizes

Particle size	Drag force (N)
6μm	3.589e-7
6-14μm	7.933e-7
14μm	1.077e-6
14-20μm	1.338e-6

The size of the particles does not affect much to change the particle trajectories and more particles are accumulated in MR and LR volume division as the carrier phase is more dominant in the domain.

4.5.3 Particle shape sensitivity

Different particle shapes are considered to understand the shape effect on the particle distribution. DEM allows modelling of different particle shapes, but in LPT, the non-spherical shape of the particles is estimated by the shape factor as described in section (2.3).

Three different shape factors namely 1, 0.85, 0.7 are simulated and compared. The closer a particle is to being isometric, better approximations are given to the drag force. Hence sphericities greater than 0.67 are considered [8]. Shape factor 1 corresponds to spherical shape, 0.85 and 0.7 correspond to an isometric cylindrical shape.

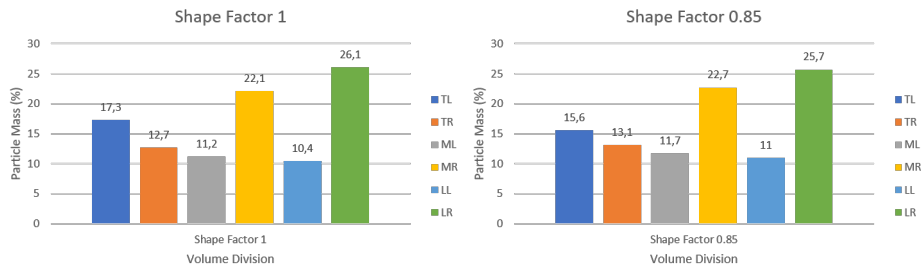


Figure 4.38: Particle mass distribution of shape factor 1

Figure 4.39: Particle mass distribution of shape factor 0.85

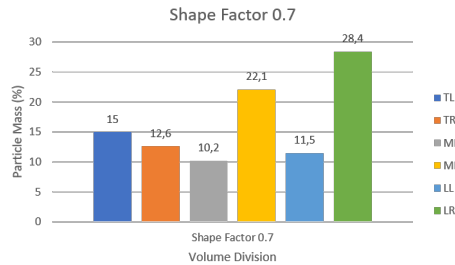


Figure 4.40: Particle mass distribution of shape factor 0.7

Figure (4.38)-(4.40) compares particle mass distribution of different shape factors. All the graphs show a similar trend where the more number of particles accumulate in the MR and LR volume divisions. Although the drag force increases as we move away from spherical shape as seen in table 4.3, the drag force is not high enough to overcome the dominant effect of the carrier phase and change the particle trajectories.

Table 4.3: Drag force comparison between different particle shapes

Shape factor	Drag force (N)
1	1.07e-6
0.85	1.21e-6
0.7	1.28e-7

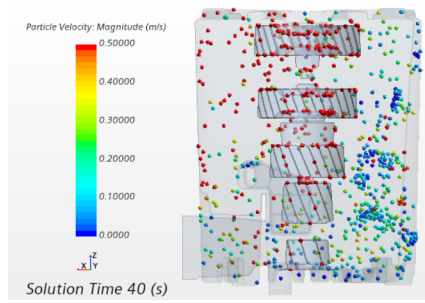


Figure 4.41: Front view Particle distribution of shape factor 1

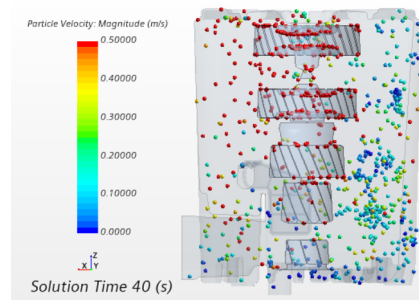


Figure 4.42: Front view Particle distribution of shape factor 0.85

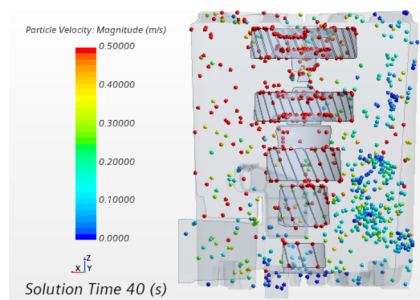


Figure 4.43: Front view Particle distribution of shape factor 0.7

Figure(4.41)-(4.43) show the particle velocity distribution in the domain. The particle distribution is less affected by particle shape. This is because the particle motion is more influenced by the continuous phase forces.

4.5.4 Gear speed

The gearbox in reality operate at various rotational speeds. Hence the particle distribution is analysed for different gear speeds (2000PRM, 1400RPM and 0RPM). The 0RPM gear speed is a special case in which the gearbox rotates at 2000RPM initially and the rotational speed is turned off before injecting the particles. The velocity contours of the three rotational speeds are shown in appendix Figure (A.24)-(A.26). The flow velocity decreases as the gear speed decreases.



Figure 4.44: Particle mass distribution of 2000RPM gear speed

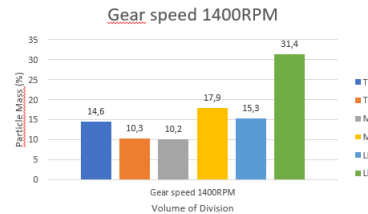


Figure 4.45: Particle mass distribution of 1400RPM gear speed

4. Results

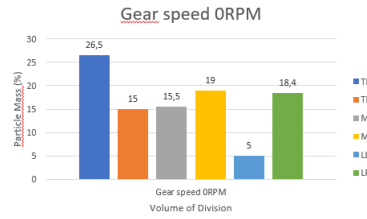


Figure 4.46: Particle mass distribution of 0RPM gear speed

Figure(4.44)-(4.46) shows the comparison of particle mass distribution of different gear speeds. The particle distribution for 2000RPM and 1400RPM follow a similar trend as before where more particles accumulate in LR and MR volume division. More particles accumulate in LR volume division in 1400RPM as the flow velocity is lesser, allowing the particles to settle in this region. The particle distribution for 0RPM gear speed is different. More Particles accumulate in TL volume division. After the particles are injected, the flow influences the particles to move towards TL volume division having higher flow velocity. Since the particle velocity decreases to almost 0 in a few time steps, the particles start to settle down in the same region.

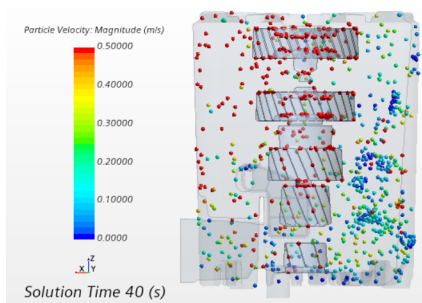


Figure 4.47: Particle velocity distribution of 2000RPM gear speed

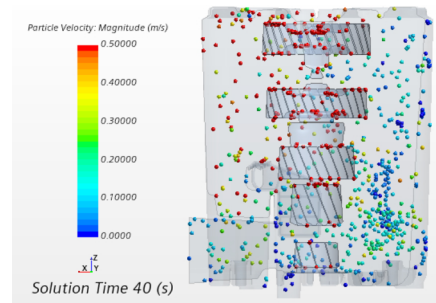


Figure 4.48: Particle velocity distribution of 1400RPM gear speed

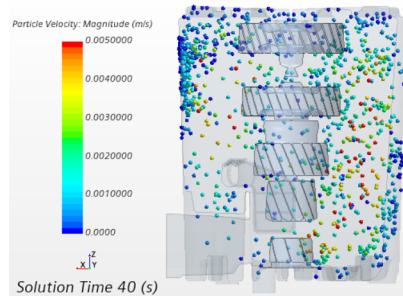


Figure 4.49: Particle velocity distribution of 0RPM gear speed

Figure(4.47)-(4.49) shows the particle velocity distribution for different gear speeds. Although maximum number of particles accumulate in TL volume division of 0RPM, Many particles also settle in the LR and MR volume division.

It can be concluded from the particle sensitivity study that all the sensitivity parameters studied have less influence on the particle mass distribution and they follow a similar trend where the particles accumulate more in the LR and MR volume division. The particles are small and cannot resist the dominant effect of the fluid flow.

4.6 Magnetic simulation

This section describe the results of the implementation of magnetic simulation in the gearbox. The test case is simulated first for simplicity and the same is applied to the gearbox model.

4.6.1 Test case

A magnetic sensitivity study is conducted to understand the influence of Remanent flux density, magnetic susceptibility and particle diameter. Laminar flow is established and a single point injector is used to inject mono-dispersed particles in the domain.

The base parameters used for the simulation of the test case is shown in table (4.4)

Table 4.4: Base parameters

Parameter	Values
μ_f	$1.2e^{-6}$ H/m
μ_m	$1.2e^{-6}$ H/m
Magnetization direction	$[0,1,0]$
Inlet velocity	0.2m/s
Particle diameter	14 μm
χ	3

4.6.1.1 Remanent flux density

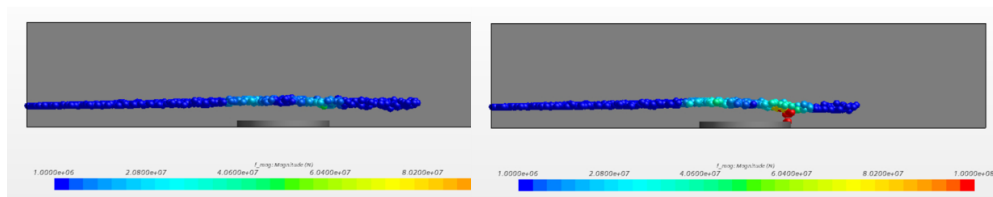


Figure 4.50: Remanent flux density: $2e^8\text{T}$ **Figure 4.51:** Remanent flux density: $3e^8\text{T}$

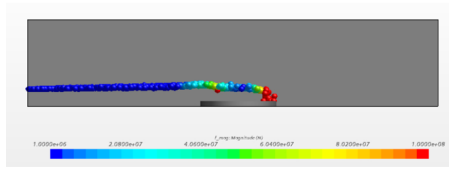


Figure 4.52: Remanent flux density: $4e^8T$

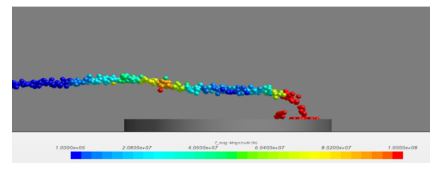


Figure 4.53: Remanent flux density: $5e^8T$

Figure (4.50)-(4.53) shows the comparison of particle attraction on the magnet for different remanent flux density (B_r). The magnetic force defined in equation (2.24) is a function of magnetic field (H) and magnetic flux density (B). Hence when the remanent flux density is increased the magnetic force on the particles also increase.

It should be noted that the realistic remanent flux density of the material is 0.3T as described in section (3.5). From figure (4.50)-(4.53), the particles are not attracted even with an unrealistic remanent flux density of $3e^8T$. Many literatures mentioned in section (1.3) develop a laminar flow of velocities in the range of 0.0001 m/s in small domains of μm range. The velocities attained in the gearbox is comparatively higher in the range of 0.2 m/s. Increase in the fluid flow velocity increases the hydrodynamic forces. The hydrodynamic forces become more dominant than the magnetic forces and the particles do not get attracted to the magnet.

Because of the time constraint and since the main focus of the thesis is to provide information regarding the best placement of the magnet and not to investigate the properties of the magnet, an unrealistic remanent flux density of $4e^8T$ is used in all the magnetic simulations as it assures that the particles are attracted to the magnet (figure (4.52)), A too high remanent flux density such as $5e^8T$ cannot be used as the magnetic forces become too great and their trajectories follow the path of the magnetic lines of force (figure (4.53)).

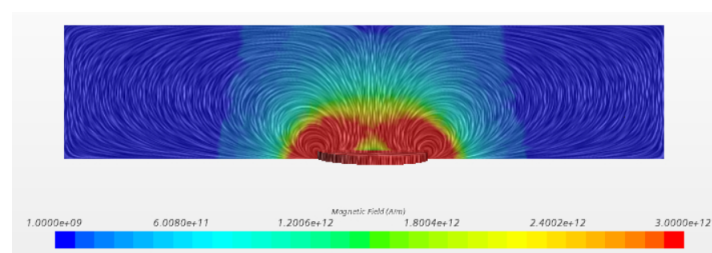


Figure 4.54: Magnetic field of the test case

The magnetic field of the test case with remanent flux density of $4e^8T$ is shown in figure (4.54). The gradient of the magnetic field is high near the magnet. The magnetic field is very high closest to the magnet and reduces considerably away from the magnet.

4.6.1.2 Magnetic susceptibility

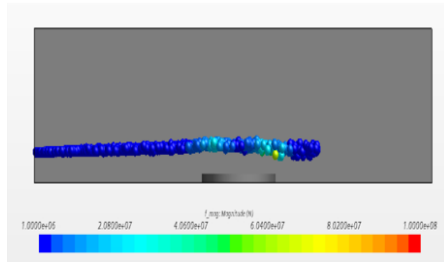


Figure 4.55: $\chi=1$

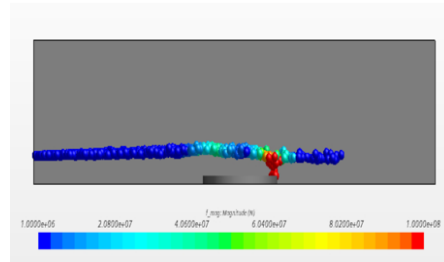


Figure 4.56: $\chi=2$

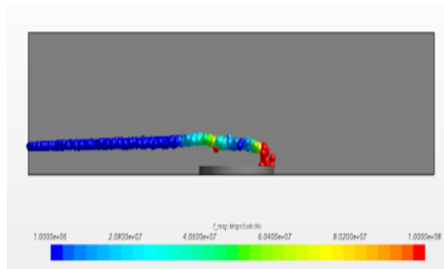


Figure 4.57: $\chi=3$

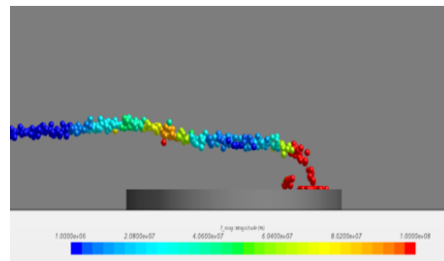


Figure 4.58: $\chi=4$

Figure (4.55)-(4.58) shows the comparison of particle attraction on the magnet for different magnetic susceptibility (χ). Three different susceptibility values with same remanent flux density of $4e^8\text{T}$ are considered for comparison. A magnetic susceptibility of 3 attracts the particles on the magnet as seen in figure (4.57). A value higher than 3 increases the degree to which the particles are magnetized in the magnetic field. This increases the magnetic force and the particles follow the path of magnetic lines of force as seen in figure (4.58).

4.6.1.3 Particle diameter

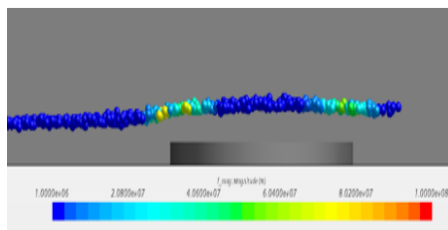


Figure 4.59: Particle diameter of $6\mu\text{ m}$

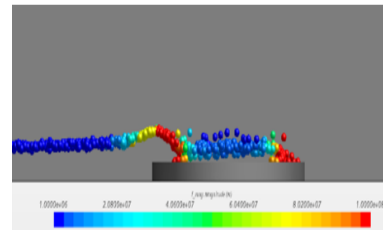


Figure 4.60: Particle diameter of $10\mu\text{ m}$

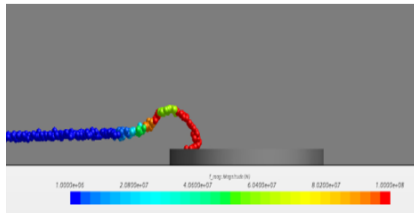


Figure 4.61: Particle diameter of $14\mu\text{m}$

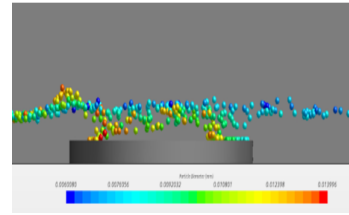


Figure 4.62: Particle diameter of $6\text{-}14\mu\text{m}$

Figure (4.59)-(4.62) shows the comparison of particle attraction on the magnet for different particle diameter. Four different particle diameters are compared with same remanent flux density of $4e^8\text{T}$ and magnetic susceptibility of 3. All the particles are attracted on the magnet for particle diameter of $14\mu\text{m}$ and no particle is attracted in the case of the smallest particle diameter of $6\mu\text{m}$. The particle size distribution of $6\text{-}14\mu\text{m}$ diameter has a mean diameter of $10\mu\text{m}$ and it can be seen in figure (4.60) that the $10\mu\text{m}$ particles are also attracted by the magnet. Figure (4.62) shows a particle size between $6\text{-}14\mu\text{m}$ being injected to the domain and smaller diameter particles are not attracted to the magnet.

The results of the test case simulation shows that a remanent flux density of $4e^8\text{T}$ and magnetic susceptibility of 3 ensures that the magnet attracts most of the particles of size distribution between $6\text{-}14\mu\text{m}$. Hence the same setup is implemented into the gearbox model.

4.6.2 Gearbox model

After investigating the particle sensitivity study in section (4.5), it is concluded that most of the particles accumulate in the LR and MR volume division. Hence, the magnet is placed in the LR volume division as a forethought of best placement of magnet to attract the particles. All the simulations are run for 40s.

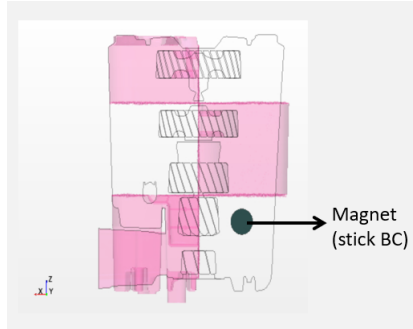


Figure 4.63: Magnet position

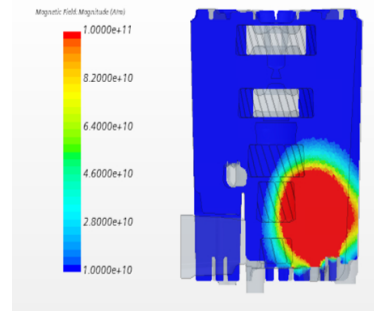


Figure 4.64: Magnetic field

Figure (4.63) shows the magnet position in the LR volume division of the gearbox. Stick boundary condition is implemented on the magnet surface. Figure (4.64) shows the magnetic field in the gearbox model with remanent flux density of $4e^8T$ and magnetic susceptibility of 3.

The magnetic sensitivity study for the gearbox model is conducted to analyse the effect of particle diameter, gear speed and magnet location on attraction of particles on the magnet.

4.6.2.1 Particle diameter

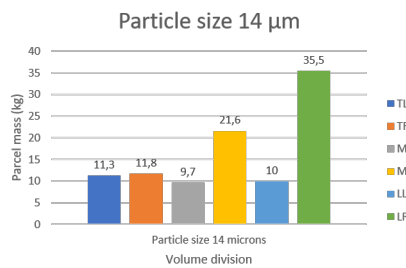


Figure 4.65: Particle mass distribution for 14 μm particle diameter

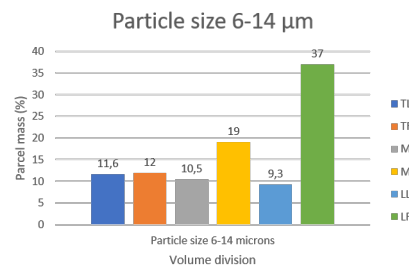


Figure 4.66: Particle mass distribution for 6-14 μm particle diameter

Figures (4.65)-(4.66) show the particle mass distribution of 14 μm and 6-14 μm particle diameters with the magnet. The figures show an increase in the percentage of particle mass in LR volume division when compared to figure (4.31) and figure (4.32) because of the magnet. The particle mass distribution of both mono-dispersed and poly-dispersed particles follow similar.

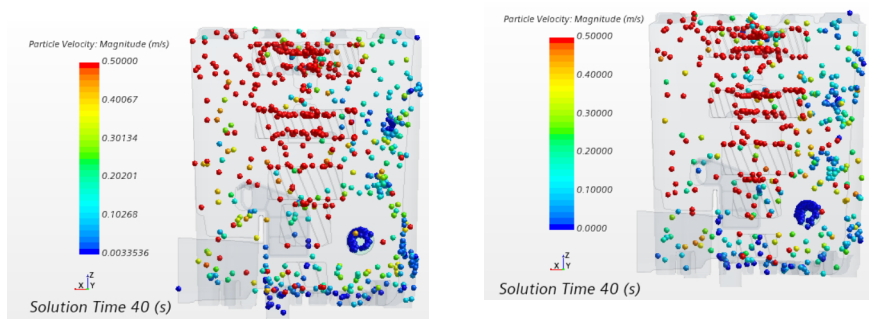


Figure 4.67: Particle velocity distribution of particle size $14\mu\text{m}$

Figure 4.68: Particle velocity distribution of particle size of $6-14\mu\text{m}$

Figure(4.67) and figure(4.68) show particle velocity distribution of both mono-dispersed and poly-dispersed particles in the domain. Figure (A.27) in appendix shows that the mono-dispersed particles are deposited on the magnet slower than the poly-dispersed particles. A comparison between only the stick boundary condition without magnetic properties and stick boundary condition with the magnetic properties is conducted to investigate that most of the particles are indeed deposited because of the magnetic properties of the magnet and not because of the stick boundary condition.

Table 4.5: Capture efficiency

Particle diameter	$14\mu\text{m}$	$6-14\mu\text{m}$
Total capture efficiency with magnetic properties	21%	29%
Total capture efficiency without magnetic properties	14%	16%
Local capture efficiency with magnetic properties	60%	78%

Table (4.5) compares the capture efficiencies of mono-dispersed and poly-dispersed particles with and without magnetic properties. The total and local capture efficiency is described in section (2.4). There is a slight increase in the capture efficiency of poly-dispersed particles because the fluid flow influences the smaller diameter particle which are not attracted by the magnet to deposit on the magnet due to stick boundary condition. Mono dispersed particle size of $6\mu\text{m}$ is not discussed as it is observed in the test case in section(4.6.1.3) that these particles are not attracted by the magnet.

4. Results

4.6.2.2 Gear speed

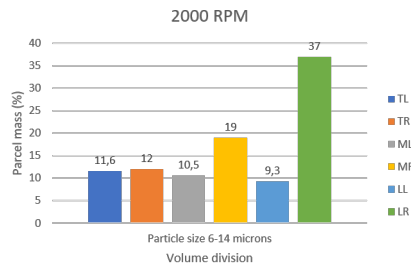


Figure 4.69: Particle mass distribution of 2000RPM gear speed

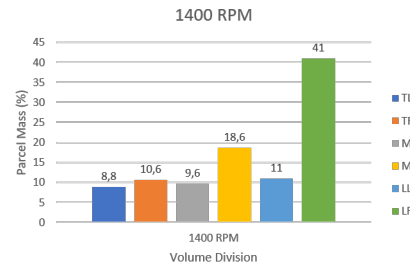


Figure 4.70: Particle mass distribution of 1400RPM gear speed

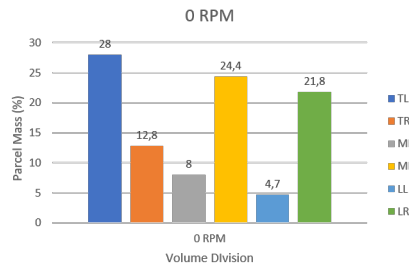


Figure 4.71: Particle mass distribution of 0RPM gear speed

Figure (4.69)-(4.71) shows the poly-dispersed particle mass distribution comparison of the three different gear speeds (2000RPM, 1400RPM and 0RPM) with the magnet. Figure (4.69) and figure (4.70) depicts an increase in the percentage of particle mass in LR volume division when compared to figure (4.44) and figure (4.45). Less particles are attracted for gear speed of 0RPM because more particles accumulate in the TL volume division and the magnet cannot attract particles in the TL volume division. Nevertheless there is a slight increase in percentage of particle mass distribution in the LR volume division.

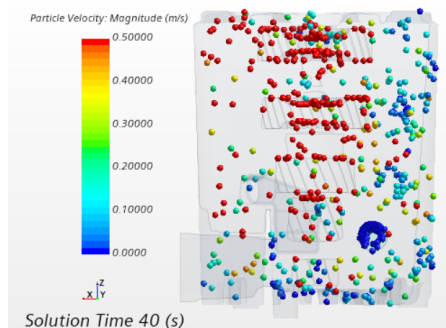


Figure 4.72: Particle velocity distribution of 2000RPM gear speed

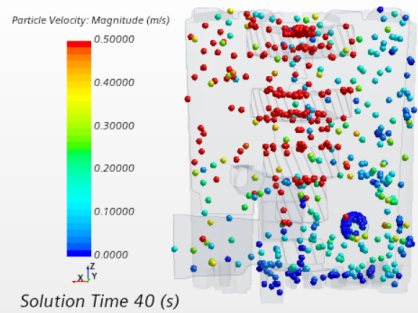


Figure 4.73: Particle velocity distribution of 1400RPM gear speed

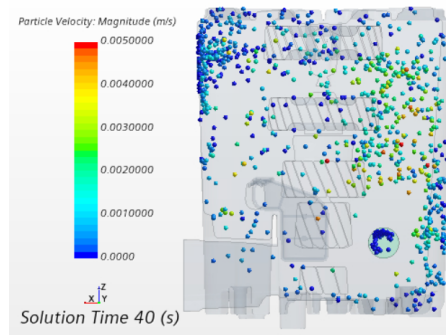


Figure 4.74: Particle velocity distribution of of 0RPM gear speed

Figure (4.72)-(4.74) shows particle velocity distribution of different gear speeds. Figure(A.28) in appendix shows a comparison plot of the particles captured on the magnet. More particles are captured as the gear speed increases as the flow influences more particles to move towards the magnet. Table (4.6) show the capture efficiency of different gear speeds. The capture efficiency decreases as the gear speed decreases. Since the flow velocity also decreases, less number of particles move close to the magnet.

Table 4.6: Capture efficiency of different gear speed

Gear speed	2000RPM	1400RPM	0RPM
Total capture efficiency	29%	28%	10%
Local capture efficiency	78%	67%	46%

4.6.2.3 Magnet position

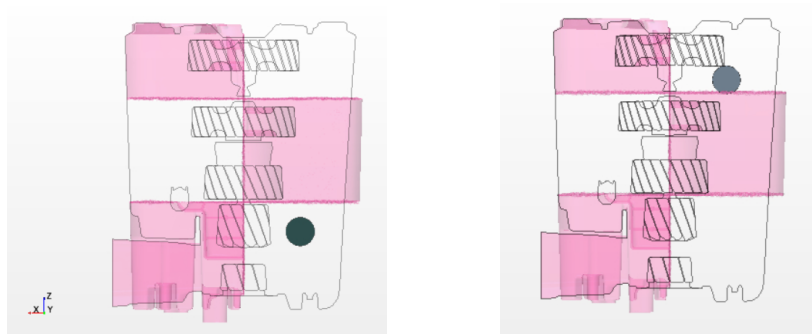


Figure 4.75: Magnet position 1 **Figure 4.76:** Magnet position 1

Figure(4.75) and figure(4.76) show two different magnet positions where in one case the magnet is placed in LR volume division with the forethought that more particles are accumulated in LR volume division and also that the flow velocity is less in LR volume division so that the particles do not need more magnetic force to overcome the hydrodynamic forces. In another case the magnet is placed in TR volume division with forethought that the magnet is closer to the injector points.

4. Results

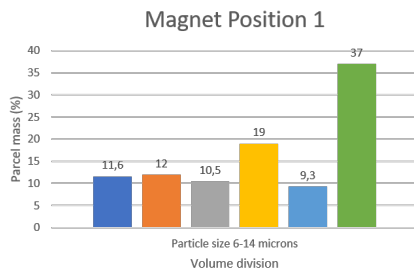


Figure 4.77: Particle mass distribution of magnet position 1

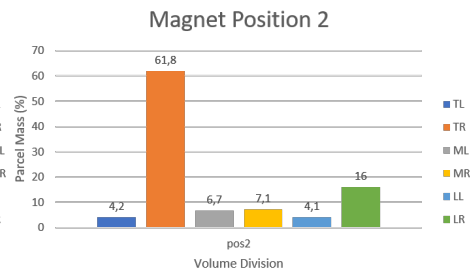


Figure 4.78: Particle mass distribution of magnet position 2

Figure (4.77) and figure (4.78) show comparison of the particle mass distribution of two different magnet position. It can be observed that the particle mass percentage in TR volume division is very high where the magnet is placed (magnet position 2).

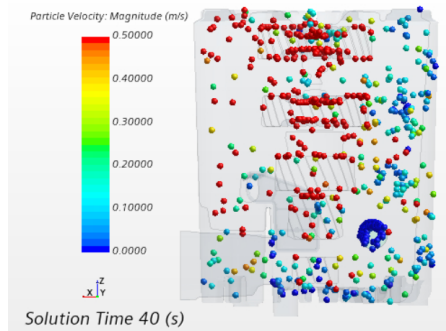


Figure 4.79: Particle velocity distribution of magnet position 1

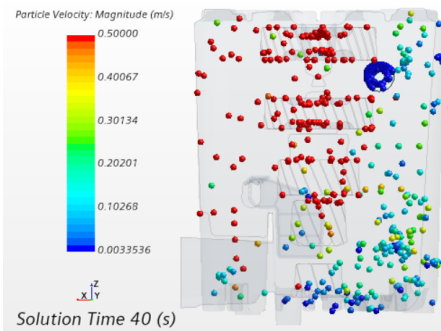


Figure 4.80: Particle velocity distribution of magnet position 2

Figure (4.79) and figure (4.80) show particle velocity distribution of the two different magnet positions. More number of particles are attracted on magnet position 2 when compared to magnet position 1. Figure (A.29) in appendix also shows that more particle mass is attracted on magnet position 2. This is because the magnet is placed closer to the particle injector positions.

Both the magnet positions are run for a longer time to analyse the maximum number of particles attracted on the magnet.

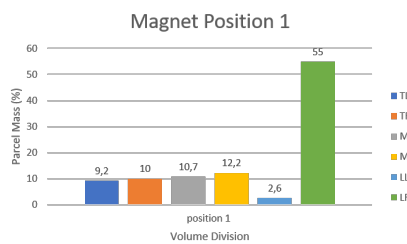


Figure 4.81: Particle mass distribution of magnet position 1

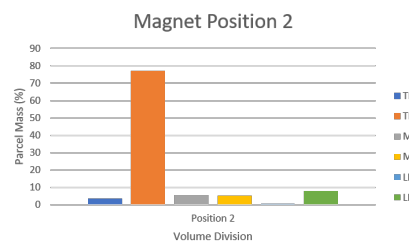


Figure 4.82: Particle mass distribution of magnet position 2

Figure (4.81) and figure (4.82) show the particle mass distribution of the two magnet positions run for a long time. The number of particles present in other volume divisions is very less when the simulation is run for a long time.

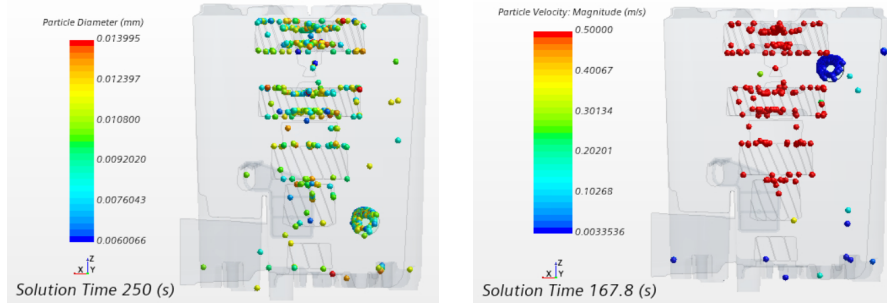


Figure 4.83: Particle velocity distribution of magnet position 1 **Figure 4.84:** Particle velocity distribution of magnet position 2

Figure (4.83) and figure (4.84) show particle velocity distribution of the two magnet positions run for a long time. Most of the particles in the domain are attracted to the magnet over long time. Particles close to the gear are not attracted as they are highly influenced by the fluid flow and cannot escape from that region. Figure (A.30) in appendix shows that The number of particles accumulating on the magnet surface increases with time and reaches a constant value. It can also be seen that particles are attracted much faster in magnet position 2 when compared to magnet position 2.

Table 4.7: Capture efficiency of different magnet positions

Magnet position	Position 1	Position 2
Total capture efficiency	29%	55%
Local capture efficiency	78%	88%
total capture efficiency (long time)	51%	72%

Table (4.7) compares the capture efficiency of the two magnet positions. maximum number of particles are attracted and the capture efficiency becomes constant when the simulation is run for a long time.

Both the magnet positions significantly captures the particles in the gearbox. Although the magnet position 2 attracts more particles when compared to magnet position 1, it is because of the particle injection sources. In reality the particle injection sources is not defined. The magnet is suggested to be positioned in last-right (LR) volume division. The flow inside the gearbox makes the particles move towards the magnet without much resistance and the magnet does not have to do much work to attract the particles. Hence, placing the magnet in LR volume division could therefore reduce the wear rate inside the gearbox

5

Conclusion

5.1 Conclusion

In this thesis, possibility of combine fluid flow and magnetic simulation in a model gearbox is investigated. The outcomes of this work is discussed in this section.

Fluid flow is developed in the gearbox using tangential velocity specification method. This method is robust and it can be easily implemented in complex domains like the gearbox model. MRF method is not an appropriate method to be implemented in this work as the gearbox is asymmetric.

Particle sensitivity analysis has been conducted with particle source location, particle size and particle shape as the parameters of interest. It is concluded that the particle distribution is less affected by the studied particle parameters and they follow a similar trend in which more particles are accumulated in MR and LR volume division. This trend is due to the dominant effect of the carrier phase.

The combination of fluid flow and magnetic simulation is first implemented in a test case for simplicity. It is observed that the hydrodynamic forces are more dominant than the magnetic forces when a realistic remanent flux density is used and the particles are not attracted to the magnet. Hence an unrealistic remanent flux density is used in all the magnetic simulations to ensure that the particles are attracted to the magnet.

The combination of fluid flow and magnetic simulation is implemented in the gearbox model. A magnetic sensitivity study is conducted to understand the effect of particle diameter, gear speed and magnet position on the capture efficiency. It is concluded that the capture efficiency of poly-dispersed particles is slightly higher than the mono-dispersed particles due to the influence of the fluid flow. For lower gear speed the capture efficiency is less due to the reduced particle movement in the domain. Although magnet position 2 captures more particles than magnet position 1, both the magnet positions investigated significantly captures the particles in the gearbox.

The magnet is suggested to be positioned in last-right (LR) volume division as more number of particles are accumulated in this region irrespective of all the different sensitivity study conducted. The flow inside the gearbox makes the particles move towards the magnet without much resistance and the magnet does not have to do much work to attract the particles. Hence placing the magnet in LR volume division could therefore reduce the wear rate inside the gearbox.

5.2 Future work

The combination of fluid flow and magnetic simulation is successfully implemented in this. For further development on this work, the magnetic properties of the particle such as magnetic susceptibility should be studied more thoroughly through experiments in devices such as vibrating sample magnetometer (VSM). Further investigation has to be carried out to implement realistic remanent flux density. Inclusion of Oil pump in the domain is interesting as it changes the flow behavior inside the domain. MRF method can be implemented in the gearbox model by considering the complete gearbox instead of a cross section of the gearbox. In addition VOF model can be incorporated into the simulation to consider the influence of air. Finally appropriate experiments have to be conducted in the actual gearbox model to validate the capture efficiency between the experiments and simulation, so that the best placement of the magnet can be finalised.

Bibliography

- [1] Hartono EA, Golubev M, Chernoray V. 'PIV Study of Fluid Flow Inside a Gearbox'. 10th International Symposium On Particle Image Velocimetry. 2013;
- [2] Franco Concli, Carlo Gorla. 'Windage, churning and pocketing losses of gears: different modelling approaches for different goals'. Received: 27 May 2016 / Published online: 22 August 2016 © Springer-Verlag Berlin Heidelberg 2016. DOI 10.1007/s10010-016-0206-9
- [3] Marc C. Keller, Samuel Braun, Lars Wieth, Geoffroy Chaussonnet, Thilo F. Dauch, Rainer Koch, Corina Schwitzke, Hans-jörg Bauer, 'Smoothed particle hydrodynamics simulation of oil-jet gear interaction'. DOI: 10.1115/1.4043640]
- [4] Carlo Gorla,¹ Franco Concli,¹ Karsten Stahl,² Bernd-Robert Hohn,² Michaelis Klaus,² Hansjörg Schultheiß,² and Johann-Paul Stemplinger², 'CFD Simulations of Splash Losses of a Gearbox'. doi:10.1155/2012/616923
- [5] H. Liu, F. Link, T. Lohner, K. Stahl, 'CFD Simulation of Geared Transmissions with Injection Lubrication'.
- [6] Franco Concli, Carlo Gorla, 'Analysis of the power losses in geared transmissions - Measurements and CFD calculations based on open source codes'. Conference Paper · August 2014
- [7] Daniel P. Anderson, P.M. O'Donnell, F Evans, 'Wear particle atlas (revised)'
- [8] Siemens PLM software. 'Start-ccm+ user guide v.2020.3'
- [9] Versteeg HK, Malalasekera W. 'An Introduction to Computational Fluid Dynamics: The Finite Volume Method'. Pearson Education
- [10] Nicole Pamme and Andreas Manz. 'On-chip-free-flow magnetophoresis: Continuous flow separation of magnetic particles and agglomerates'. doi:10.1021/ac049183o
- [11] Saud A. Khashan, Anas Alazzam, Bobby Mathew, Sawsan Dagher and Mohammad Hamdan. 'CFD Simulation of magnetic separation in microfluidics systems using mixture model'. Eleventh international conference on CFD in the minerals and process industries CSIRO, Melbourne, Australia, 7-9 December 2015.
- [12] Saud A. Khashan, Edward P. Furlani. 'Scalability analysis of magnetic bead separation in a microchannel with an array of soft magnetic elements in a uniform magnetic field'. <https://doi.org/10.1016/j.seppur.2014.02.007>
- [13] Saud A. Khashan, Emad Elnajjar and Yousef Haik. 'CFD simulation of the magnetophoretic separation in a microchannel'. doi:10.1016/j.jmmm.2011.06.001
- [14] Jin-Woo Choi, Chong.H.Ahn, Shekhar Bhansali.H and Thurman

- Henderson. 'A new magnetic bead-based, filterless bio-separator with planar electromagnet surfaces for integrated bio-detection systems'. [https://doi.org/10.1016/S0925-4005\(00\)00458-5](https://doi.org/10.1016/S0925-4005(00)00458-5).
- [15] Saud A. Khashan and Edward P. Furlani. 'Effects of particle-fluid coupling on particle transport and capture in a magnetophoretic microsystem'. DOI 10.1007/s10404-011-0898-y
- [16] Dr. Vasile Murariu, Metso Minerals industries, Technology development, Colorado springs, Colorado, USA. 'Simulating a low intensity magnetic separator model (LIMS) using DEM, CFD and FEM magnetic design software'.
- [17] Feiwang Wang, Hongming Zhao, Huixin Dai and Wuxing Du. 'Fully coupled multi-physics modeling of the multi-type magnetic particles dynamic behavior in low intensity magnetic separator'. DOI: 10.5277/ppmp18117.
- [18] Sato Y. 'Turbulence structure and modeling of dispersed two-phase flows'. Keio: PhD thesis, Keio University, Japan.
- [19] Elghobashi SE. 'On predicting particle-laden turbulence flows. Appl Sci Res 52:309-329.
- [20] Crowe CT, Troutt TR, Chung JN. 'Numerical models for two phase turbulent flows'. Annu Rev FluidMech 28:11-43.
- [21] Kohnen, G. Ruger M and Sommerfeld M. 'Convergence behavior for numerical calculations by the euler/Lagrange method for strongly coupled phases'. FED-vol185, Numerical methods in multiphase flows ASME 1994.
- [22] Martin R. Maxxey and James J. Riley. 'Equation of motion for a small rigid sphere in a nonuniform flow'. Received 11 june 1982, accepted 22 november 1982.
- [23] Iowa state university. Center for Nondestructive evaluation. nde-ed.org/Physics/Magnetism/LongFields.
- [24] <https://www.livescience.com/38059-magnetism.html>.
- [25] <https://www.emfs.info/what/terminology/field-flux/>
- [26] <https://www.differencebetween.com/difference-between-magnetic-permeability-and-vs-susceptibility>
- [27] Bomatec. <https://www.bomatec.com/wp-content/uploads/2019/01/BMFpa-1222H.pdf>
- [28] Antonio Pascau, Carlos Pérez, Francisco José Serón. 'A comparison of segregated and coupled methods for the solution of the incompressible Navier-Stokes equations'. [https://doi.org/10.1002/\(SICI\)1099-0887\(199610\)12:10<617::AID-CNM10>3.0.CO;2-J](https://doi.org/10.1002/(SICI)1099-0887(199610)12:10<617::AID-CNM10>3.0.CO;2-J)

A

Appendix 1

Mesh study

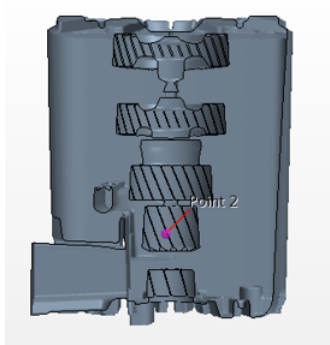


Figure A.1: Location of point for velocity and pressure plot

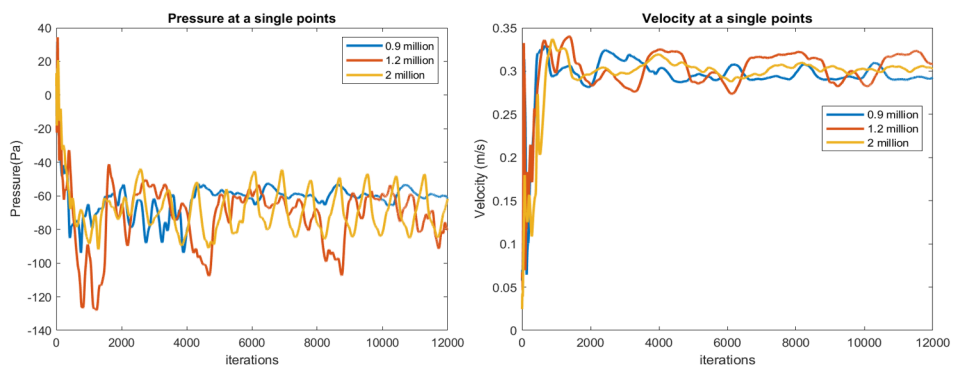


Figure A.2: Pressure plot

Figure A.3: velocity plot

Single phase flow

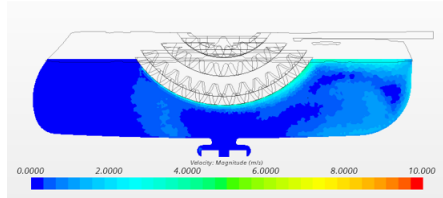


Figure A.4: Method 1: Velocity contour (plane 1)

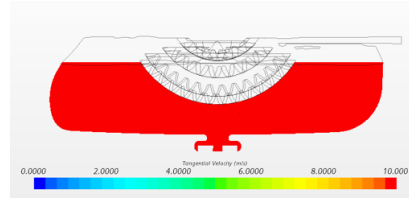


Figure A.5: Method 2: Velocity contour (plane 1)

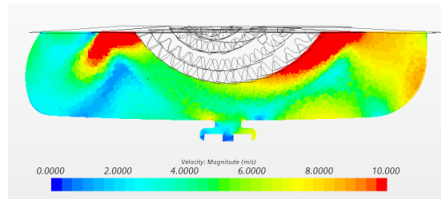


Figure A.6: Method 3: Velocity contour (plane 1)

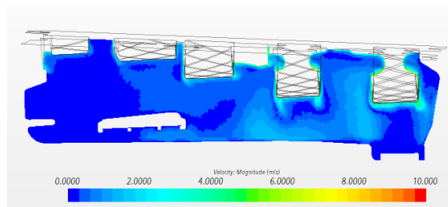


Figure A.7: Method 1: Velocity contour (plane 2)

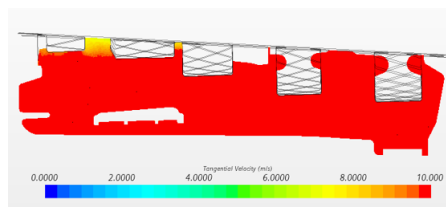


Figure A.8: Method 2: Velocity contour (plane 2)

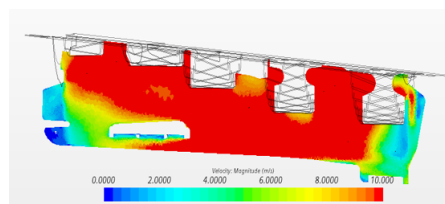


Figure A.9: Method 3: Velocity contour (plane 2)

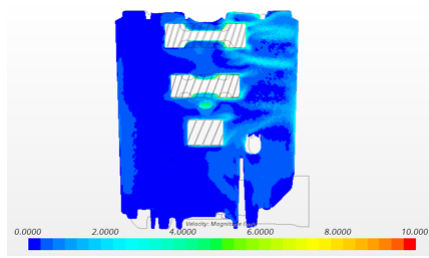


Figure A.10: Method 1: Velocity contour (plane 3)

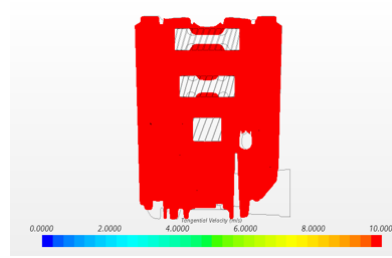


Figure A.11: Method 2: Velocity contour (plane 3)

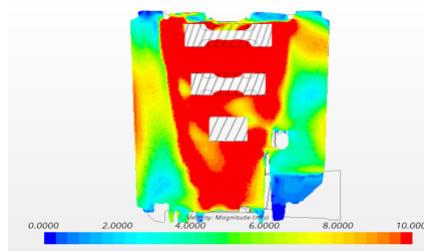


Figure A.12: Method 3: Velocity contour (plane 3)

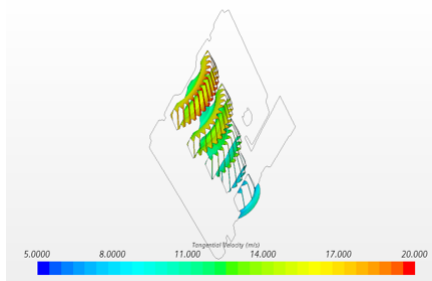


Figure A.13: Method 1: Tangential gear velocity

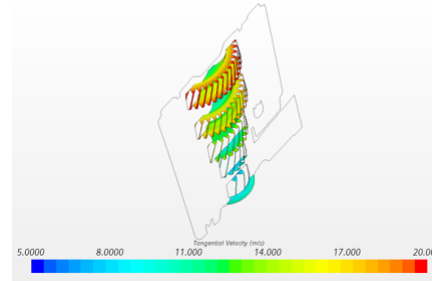


Figure A.14: Method 2: Tangential gear velocity

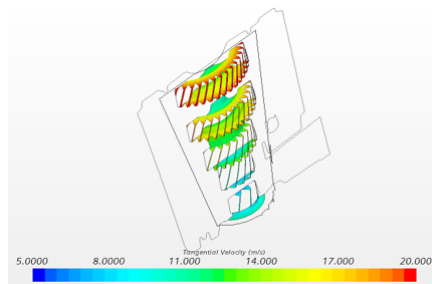


Figure A.15: Method 3: Tangential gear velocity

Unsteady simulation

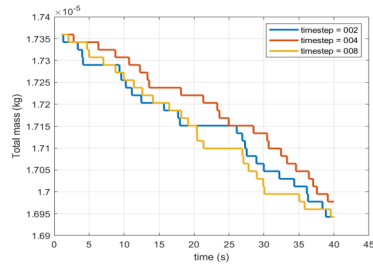


Figure A.16: time vs total particle mass

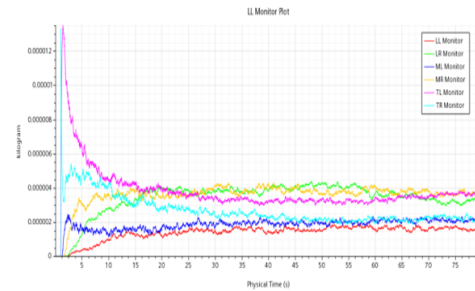


Figure A.17: Particle distribution in each volume division

Particle source analysis

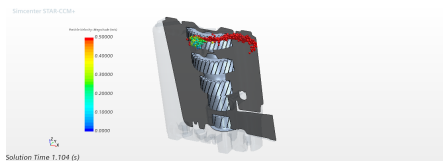


Figure A.18: ISO view of particle distribution of injector 0 at first time step

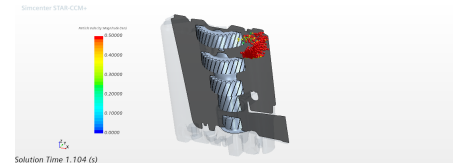


Figure A.19: ISO view of particle distribution of injector 1 at first time step

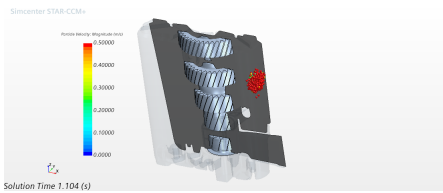


Figure A.20: ISO view of particle distribution of injector 2 at first time step



Figure A.21: ISO view of particle distribution of injector 3 at first time step

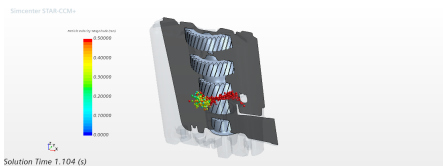


Figure A.22: ISO view of particle distribution of injector 4 at first time step

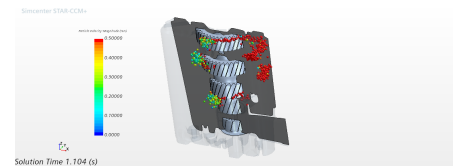


Figure A.23: ISO view of particle distribution of multiple injector at first time step

Gear speed

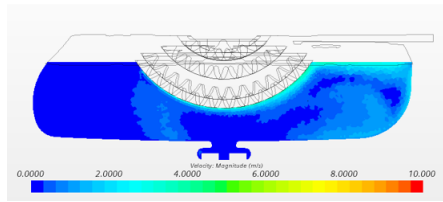


Figure A.24: Gear speed: 2000RPM

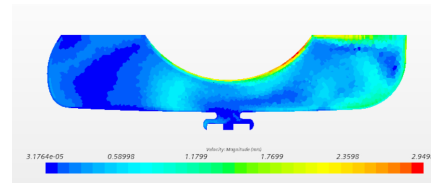


Figure A.25: Gear speed: 1400RPM

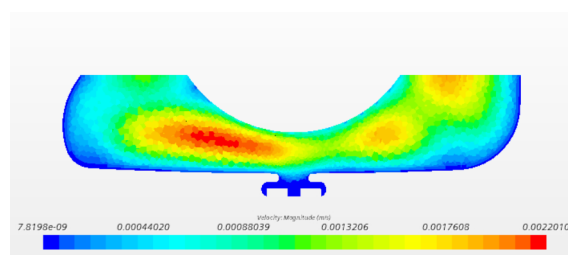


Figure A.26: Gear speed: 0RPM

Magnetic simulation (Particle diameter)

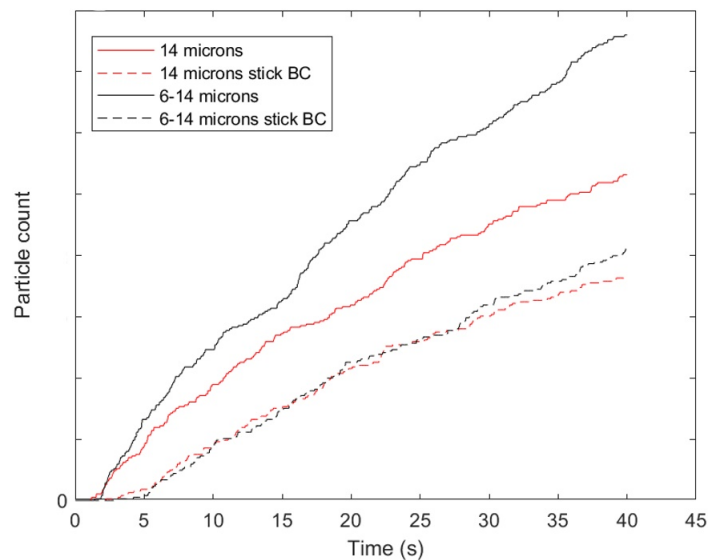


Figure A.27: Plot of comparison of particle count with different BC and particle diameters

Magnetic simulation (Gear speed)

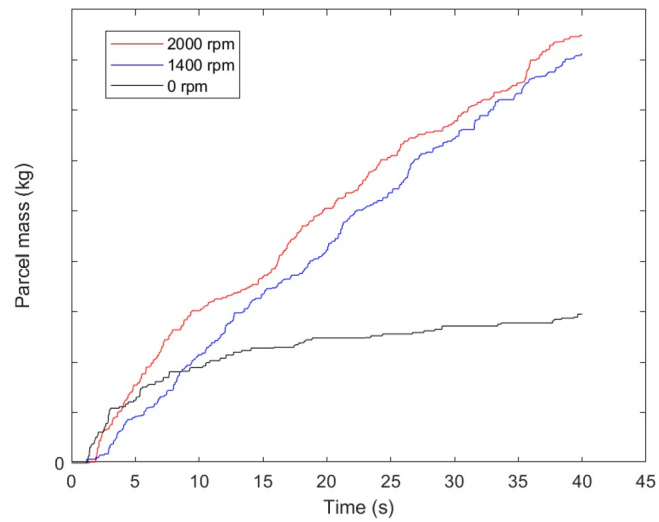


Figure A.28: Plot of comparison of particle count with gear speed

Magnetic simulation (magnet position)

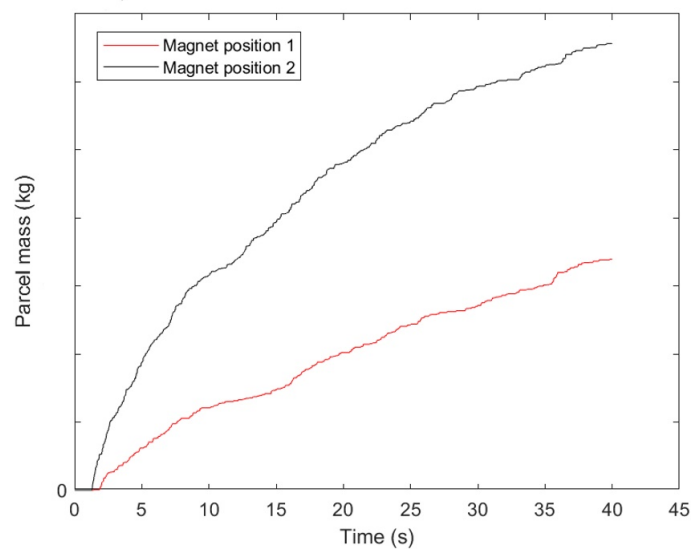


Figure A.29: Plot of comparison of particle count with magnet position

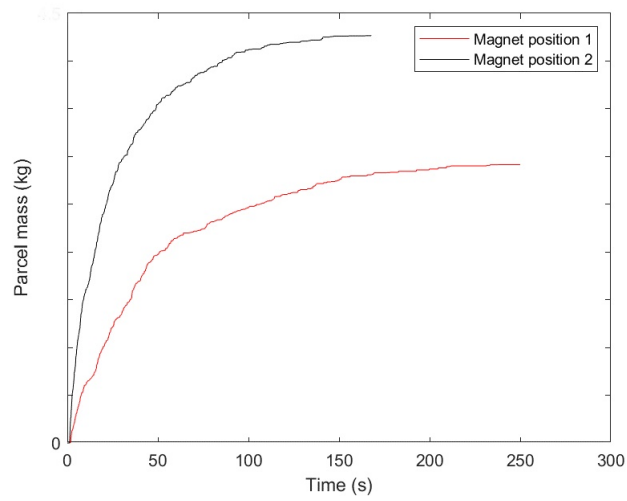


Figure A.30: Plot of comparison of particle count with magnet position (long time simulation)

DEPARTMENT OF MECHANICS AND MARITIME SCIENCES
CHALMERS UNIVERSITY OF TECHNOLOGY
Gothenburg, Sweden
www.chalmers.se



CHALMERS
UNIVERSITY OF TECHNOLOGY